Measurement of the Top Quark Mass from the Invariant Mass of the Top-Antitop Quark System with the CMS Experiment

von

Andreas Hinzmann

Diplomarbeit in Physik

Contents

1 Introduction

In 2008 the world's largest proton-proton collider, the Large Hadron Collider (LHC), will start operations. It was built for center-of-mass energies up to 14 TeV to clarify several fundamental questions in high energy physics.

For many years the Standard Model of elementary particles has proved to give a very good description of all particles below the size of a proton and their interactions. But up to now an important part of the Standard Model, the Higgs boson, has not been observed. The search for the Higgs boson and physics beyond the Standard Model will be the main challenges for the LHC.

However, the LHC will also allow to test the Standard Model with high precision and constrain the area for new physics. The heaviest of all quarks, the top quark, has a strong coupling to the Higgs boson. A precision measurement of the top quark mass will thus together with the mass of the W boson constrain the allowed range for the mass of the Higgs boson.

By now the Tevatron proton-antiproton collider is the only collider which allows the production of top quarks and a measurement of the top quark mass. The discovery of the top quark in 1995 at the Tevatron by the CDF and DØ experiments was a great success for the Standard Model which made its prediction 17 years before.

The LHC will be able to produce orders of magnitude more top quarks than the Tevatron. This will allow precision measurements of the properties of the top quark.

In this work a new method to measure the top quark mass is studied. This method relies on the high number of top quarks produced at the LHC. The invariant mass distribution of the top-antitop quark system is used to extract the top quark mass. In principle the invariant mass contains twice the top quark mass information. Hence the top quark mass can be extracted from the shape of the invariant mass spectrum.

This study aims to clarify if such a measurement of the top quark mass is possible and to estimate the expected experimental uncertainties. The study is carried out for the CMS experiment, one of the two general purpose detectors installed at the LHC.

The structure of this report is as follows. Chapter 2 gives a short review of the Standard Model of elementary particle physics. In Chapter 3 the top quark and its mass as well as the invariant mass of the top-antitop quark system are introduced. Chapter 4 gives a small introduction to event generators. An overview on the LHC and the CMS experiment will be given in Chapter 5. The detector simulation, event reconstruction and analysis software will be described in Chapter 6. Chapter 7 will explain the data samples used in the analysis as well as the event pre-selection. The description of the analysis follows in Chapters 8 and 9. Chapter 8 will describe how the invariant mass of the top-antitop quark system can be reconstructed. And Chapter 9 explains how the top quark mass is extracted from the invariant mass spectrum. Finally a summary is given in Chapter 10.

1 Introduction

2 The Standard Model of Elementary Particles

The Standard Model (SM) of elementary particle physics describes the structure and interactions of small-scale particles [1,2]. Its predictions have been tested with very high precision and up to the present it endured all experimental checks.

The SM consists of a set of point-like particles and interactions between these particles. According to the SM all matter is made from these particles and in principle all interaction of matter can be understood from the interaction of its point-like building blocks.

Force	Range [m]	Relative strength	Force carrier	Mass [GeV/c^2]	'Charge'
Strong force	10^{-15}	1	8 gluons (g)	massless	color
Electromagnetic force	inf	10^{-2}	photon (γ)	massless	charge
Weak force	10^{-13}	10^{-2}	$W^\pm$	80.403 ± 0.029	weak-isospin
			Z^0	91.1876 ± 0.0021	

Table 2.1: The three forces described by the Standard Model. The masses correspond to the force carrying bosons and are taken from Ref. [3].

The three forces described by the SM are summarized in Table 2.1. The electromagnetic force is responsible, for example, for the emission of light from excited atoms. The most famous effect of the weak force is the nuclear beta decay. The strong force holds nuclei together.

The fourth force in nature, the gravitational force, is not described by the SM. However, its impact on elementary particles is very small since its relative strength compared to the strong force is of order 10^{-39}. Anyway, the search for a theory including all four forces is one of the most interesting challenges of nowadays physics.

In the SM the interactions are described by quantum gauge field theories. In these theories the forces are said to be due to the exchange of field quanta, which mediate the forces. These field quanta have spin 1 and are called gauge bosons. As presented in Table 2.1 the electromagnetic force is mediated by the photon, the weak force by the $W^\pm$ and Z^0 bosons and the strong force by 8 gluons.

Table 2.1 also summarizes which 'charge' is responsible for interaction of particles with the three forces. For the electromagnetic force the responsible quantum number is the charge of a particle. The so called weak-isospin is introduced for the weak force. The counterpart of the

charge for the strong force is called color. These quantum numbers will be explained in detail in Sections 2.2.1 and 2.2.2.

In the following three sections the particles and interactions of the SM as well as the so called Higgs mechanism, which gives rise to particle masses in the SM, will be described.

From here on, natural units will be used, $\hbar = c = 1$, which means that $[\text{mass}] = [\text{energy}] = [\text{momentum}] = \frac{1}{[\text{length}]} = \frac{1}{[\text{time}]}$.

2.1 The Elementary Particles

The elementary particles of the SM can be divided in two classes: the above mentioned gauge bosons with spin 1 which mediate the forces and the spin 1/2 particles, the fermions, of which matter is composed.

Particle	Gene-ration	Mass [MeV/c^2]	Charge (Q)	3$^{\text{rd}}$ component of weak-isospin (T_3)	Color
Electron (e^-)	1	0.511	-1	+1/2	
Electron neutrino (ν_e)	1	$< 2 \times 10^{-6}$	0	-1/2	
Muon (μ^-)	2	106	-1	+1/2	
Muon neutrino (ν_μ)	2	< 0.19	0	-1/2	
Tau (τ^-)	3	1777	-1	+1/2	
Tau neutrino (ν_τ)	3	< 18.2	0	-1/2	
Up quark (u)	1	1.5-3	+2/3	-1/2	rgb
Down quark (d)	1	3-7	-1/3	+1/2	rgb
Charm quark (c)	2	$(1.25 \pm 0.09) \times 10^3$	+2/3	-1/2	rgb
Strange quark (s)	2	70-120	-1/3	+1/2	rgb
Top quark (t)	3	$(170.9 \pm 1.8) \times 10^3$ [4]	+2/3	-1/2	rgb
Bottom quark (b)	3	$(4.20 \pm 0.07) \times 10^3$	-1/3	+1/2	rgb

Table 2.2: Leptons and quarks and their properties. Masses are taken from Ref. [3] if not stated differently. The third component of the weak-isospin is stated for left-handed particles only. 'rgb' in the last column shall indicate that the quarks exist in three different color states 'red', 'green' and 'blue'.

Table 2.2 gives a summary of the fermions in the SM. They can be grouped into leptons and quarks. There are 6 leptons (e^-, ν_e, μ^-, ν_μ, τ^-, ν_τ) and their corresponding antiparticles (e^+, $\bar{\nu}_e$, μ^+, $\bar{\nu}_\mu$, τ^+, $\bar{\nu}_\tau$). There are also 6 quarks (u, d, c, s, t, b) and antiquarks ($\bar{u}, \bar{d}, \bar{c}, \bar{s}, \bar{t}, \bar{b}$). While quarks participate in all three interactions, leptons do not participate in the strong interaction since they do not carry color charge. Within the leptons, the neutrinos play a special role. Since they carry neither charge nor color, they take part only in weak interactions which makes their detection very challenging.

Both the leptons and the quarks can be grouped into three generations as shown in Table 2.2. When looking at the particle masses a clear hierarchy of the three generation attracts attention.

This hierarchy is not explained by the SM and is one of the open questions in particle physics. As a consequence of the mass hierarchy, most of the matter surrounding us consists of fermions from the first generation because they cannot decay any further. Atoms, for example, consist of nucleons formed by up and down quarks which is surrounded by electrons. Heavy particles such as the top quark can only be observed in physics experiments having sufficient energies for producing their particle masses.

2.2 The Interactions

2.2.1 The Electroweak Interaction

The electromagnetic and the weak force can be described in one quantum field theory. This theory is named Glashow-Weinberg-Salam model after its developers.

In the Glashow-Weinberg-Salam model fermions are represented by spinor fields ψ. Since the weak force only acts on left-handed fermions, the fermions are separated in left-handed fields (with $\psi_L = \frac{1}{2}(1 - \gamma_5)\psi$) and right-handed fields (with $\psi_R = \frac{1}{2}(1 + \gamma_5)\psi$). The left-handed fermions are grouped into weak-isospin doublets while the right-handed fermions form singlets:

$$\begin{pmatrix} u \\ d \end{pmatrix}_L \Bigg| \begin{pmatrix} c \\ s \end{pmatrix}_L \Bigg| \begin{pmatrix} t \\ b \end{pmatrix}_L \Bigg| \begin{pmatrix} \nu_e \\ e \end{pmatrix}_L \Bigg| \begin{pmatrix} \nu_\mu \\ \mu \end{pmatrix}_L \Bigg| \begin{pmatrix} \nu_\tau \\ \tau \end{pmatrix}_L$$

$$\begin{array}{c|c|c|c|c|c} u_R & c_R & t_R & & & \\ d_R & s_R & b_R & e_R & \mu_R & \tau_R \end{array}$$

All fermions are classified by two quantum numbers which define their characteristics in electroweak interactions: the third component of the weak-isospin T_3 and the weak hypercharge Y. In each doublet the upper element has $T_3 = -\frac{1}{2}$ and the lower element $T_3 = +\frac{1}{2}$. The hypercharge is given by the relation $Y = 2(Q - T_3)$, where Q is the charge.

Right-handed neutrinos are not listed because neutrinos were assumed to be massless in the original SM. Recent measurements have, however, shown that they indeed have a small mass.

The dynamics of electroweak forces can be derived from the free particle Lagrangian by demanding invariance under gauge transformations of $SU(2)_L \times U(1)_Y$. The free particle Lagrangian is given by

$$\mathcal{L}_0 = i\bar{\psi}\gamma^\mu \partial_\mu \psi \ . \tag{2.1}$$

The generators of the $SU(2)_L$ and $U(1)_Y$ are $\vec{T} = (T_1, T_2, T_3)^T$ and Y where the T_i follow the commuting relations $[T_i, T_j] = i\varepsilon_{ijk}T_k$. The Lagrangian is then demanded to be invariant under the transformations

$$\psi_L \rightarrow e^{ig\vec{\alpha}(x)\vec{T} + ig'\beta(x)Y}\psi_L \tag{2.2}$$

$$\psi_R \rightarrow e^{ig'\beta(x)Y}\psi_R \ . \tag{2.3}$$

To ensure the invariance under these transformations (the gauge invariance) additional terms have to be added to the free Lagrangian. These terms involve the spin 1 fields $\vec{W}_\mu = (W_{1\mu}, W_{2\mu}, W_{3\mu})^T$ and B_μ which in principle correspond to the above mentioned gauge bosons that mediate the forces ($W^\pm, Z^0, \gamma$). The resulting Lagrangian is then

$$\mathcal{L}_{EW} = \sum_{fermions} (i\bar{\psi}_L\gamma^\mu[\partial_\mu + ig\vec{W}_\mu\vec{T} + ig'Y_L\frac{1}{2}B_\mu]\psi_L + i\bar{\psi}_R\gamma^\mu[\partial_\mu - ig'Y_R\frac{1}{2}B_\mu]\psi_R)$$

$$-\frac{1}{4}\vec{W}_{\mu\nu}\vec{W}^{\mu\nu} - \frac{1}{4}B_{\mu\nu}B^{\mu\nu} \quad (2.4)$$

where $D_\mu = \partial_\mu + ig\vec{W}_\mu\vec{T} + ig'Y\frac{1}{2}B_\mu$ is called the covariant derivative.

2.2.2 The Strong Interaction

The quantum field theory that describes the strong interaction is called Quantum Chromodynamics (QCD). Similarly to the electroweak theory the Lagrangian can be derived from a gauge group which is $SU(3)_C$ for QCD.

In QCD the quarks are grouped in color triplets. Each quark carries one of the three different color charges which are called 'red', 'green' and 'blue'. Antiquarks carry the corresponding anti-colors. Leptons do not carry color charge and thus do not participate in strong interactions.

The gauge bosons in QCD are eight gluons. In contrast to electroweak theory, the gluons carry color charges themselves: one unit of color and one unit of anticolor. As a consequence gluons couple not only to quarks but also to themselves.

In nature free quarks cannot be observed. It is an experimental fact that only combinations of quarks that form a color singlet state are observed. The possible states are hadrons and mesons, $\varepsilon_{ijk}q_iq_jq_k$, $\varepsilon_{ijk}\bar{q}_i\bar{q}_j\bar{q}_k$ and $\bar{q}^iq_i$, where i, j, k are colors.

In contrast to electroweak theory, the coupling strength of QCD is very strong. Weak couplings guarantee a good description in perturbation theory with limited order. However, perturbative calculations in QCD are limited to interactions with high momentum transfer.

2.3 The Higgs Mechanism

The Higgs mechanism, which is named after its inventor Peter Higgs, gives rise to particle masses in the SM. The particles described in electroweak theory, e.g. the gauge bosons $\vec{W}_\mu$ and B_μ, are massless. Mass-terms such as $\frac{1}{2}M^2B_\mu B^\mu$ cannot be added since the Lagrangian including them is not gauge invariant. To solve this problem the Higgs mechanism is introduced.

A new scalar field of the form $\vec{\phi} = \begin{pmatrix} \phi_1 + i\phi_2 \\ \phi_3 + i\phi_4 \end{pmatrix}$ is introduced and a new term $\mathcal{L}_H$ is added to the Lagrangian:

$$\mathcal{L}_H = |D_\mu\vec{\phi}|^2 - V(\vec{\phi}^\dagger\vec{\phi}) \quad (2.5)$$

$$V(\vec{\phi}^\dagger\vec{\phi}) = \mu^2\vec{\phi}^\dagger\vec{\phi} + \lambda(\vec{\phi}^\dagger\vec{\phi})^2 . \quad (2.6)$$

The term $V(\vec{\phi}^\dagger \vec{\phi})$ is called the Higgs potential which is given by two the parameters μ^2 and λ.

By choosing the parameters $\mu^2 < 0$ and $\lambda > 0$ the vacuum expectation value (or ground state) of the Higgs potential $V(\vec{\phi}^\dagger \vec{\phi})$ is different from zero. If the fields ϕ_i ($i = 1, 2, 3, 4$) are then redefined in such a way that their vacuum expectation value is zero, one gets three massless fields and one massive field, the so called Higgs boson field. This mechanism is called spontaneous symmetry breaking. In principle both parameterizations of the fields ϕ_i ($i = 1, 2, 3, 4$) describe the same physics. However, since we calculate in perturbation theory with limited order, only the parametrization with the vacuum expectation value equal to zero will give correct results.

When spontaneous symmetry breaking is applied, the fields $\vec{W}_\mu$ and B_μ transform into four new massive fields $W_\mu^\pm$, Z_μ^0 and the massless photon field A_μ. They are connected by the following relations:

$$\begin{pmatrix} A_\mu \\ Z_\mu^0 \end{pmatrix} = \begin{pmatrix} \cos\theta_W & \sin\theta_W \\ -\sin\theta_W & \cos\theta_W \end{pmatrix} \begin{pmatrix} B_\mu \\ W_\mu^3 \end{pmatrix} \tag{2.7}$$

$$W_\mu^\pm = \frac{1}{\sqrt{2}}(W_\mu^1 \mp iW_\mu^2) \,. \tag{2.8}$$

Here θ_W is the Weinberg angle, which is defined by the coupling constants $g'/g = \tan\theta_W$.

The masses of fermions are also generated by spontaneous symmetry breaking by adding Yukawa interaction terms of the fermions with the Higgs field. This introduces new massive fields, the so called mass eigenstates of the original fermions (the electroweak eigenstates). For quarks these two states differ. When one sets the weak eigenstates of the up-type quarks equal to their mass eigenstates, the relation between the two states of the down-type quarks are given by

$$\begin{pmatrix} d' \\ s' \\ b' \end{pmatrix} = \begin{pmatrix} V_{ud} & V_{us} & V_{ub} \\ V_{cd} & V_{cs} & V_{cb} \\ V_{td} & V_{ts} & V_{tb} \end{pmatrix} \begin{pmatrix} d \\ s \\ b \end{pmatrix} \,. \tag{2.9}$$

This matrix V is called the Cabbibo-Kobayashi-Maskawa (CKM) matrix.

As a consequence the massive quarks observed in nature behave as mixtures of weak eigenstates. Weak interactions can thus lead to transitions between different quark generations. In principle the same applies to leptons. Since neutrinos are regarded as massless in the SM, mixing of flavors is not allowed for leptons. Extensions to the SM are needed in order to explain the results of neutrino oscillation experiments published in recent years.

3 The Top Quark

The top quark is the heaviest of all six quarks and forms a weak-isospin doublet with the bottom quark [1,5]. The discovery of the bottom quark in 1977 strongly suggested the existence of a sixth quark. The discovery of the top quark in 1995 by the CDF and DØ experiments at the Fermi National Accelerator Laboratory (Fermilab) Tevatron [6,7] was thus a great success for the Standard Model.

Due to its high mass which is close to the scale of electroweak symmetry breaking the top quark may play a special role in nature. Another point that makes the study of the top quark a very interesting topic is that it has a strong coupling to the yet unobserved Higgs boson. Therefore, exact measurements of the mass of the top quark provide strong constraints on the Higgs boson mass. Precision measurements of the top quark mass are currently carried out at the Tevatron and will be an interesting topic for studies at the LHC.

In the next two sections the production of top quarks at hadron colliders and their decay will be described. In Section 3.3 the top quark mass and its measurements will be discussed. This is followed by an introduction to the invariant mass of the top-antitop quark system in Section 3.4.

3.1 Top Quark Production at Hadron Colliders

The production of top quarks at hadron colliders with proton-antiproton (Tevatron) or proton-proton (LHC) collisions can be described by perturbative QCD.

In the common approach, the production is factorized in two parts. The first part, the parton distribution functions (PDFs), describe the probability for interaction with highly energetic partons (quarks or gluons) from the protons. The second part is the production of a top-antitop ($t\bar{t}$) pair from two highly energetic partons which can be calculated in perturbative QCD. This factorization approach is depicted in Figure 3.1.

The model which is used in the factorization approach for the interaction of two protons is the so called parton model. In this model the proton consists of partons (quarks and gluons). In momentum space, the composition of the proton varies with time and the energy at which it is probed. Up to the present the exact composition could not be computed in QCD. However, one can determine from measurements of the proton structure functions, the probability density to observe a parton of flavor i carrying the longitudinal momentum fraction x_i in a proton when probed at a scale μ_F, the so called parton distribution functions (PDFs), $f_i(x_i, \mu_F)$. They have been parametrized and extracted from global QCD fits to data from high energy scattering experiments. In Figure 3.2 the PDFs of one example parametrization are shown.
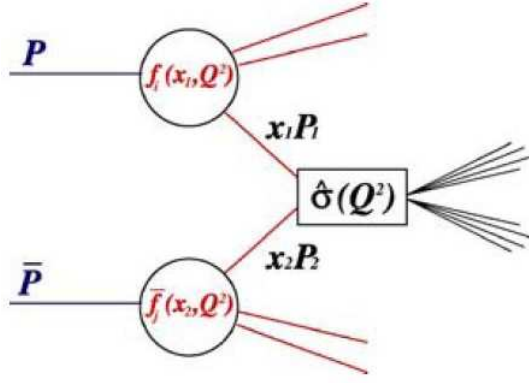
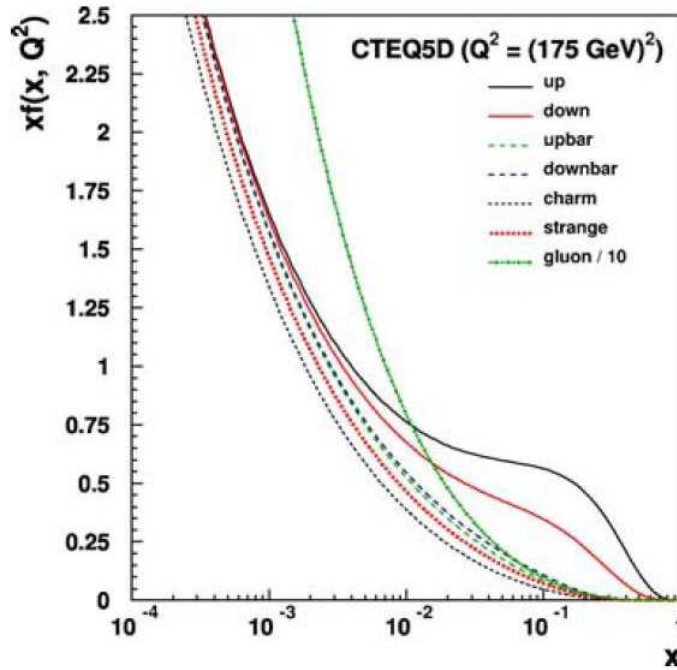Figure 3.1: Factorization approach for $t\bar{t}$ production [5].

Figure 3.2: The PDFs from the CTEQ5D [8] parametrization.

The total cross section for $t\bar{t}$ production in proton-proton collisions can be calculated as:

$$\sigma^{t\bar{t}}(\sqrt{s}, m_{top}) = \sum_{i,j=q,\bar{q},g} \int dx_i dx_j f_i(x_i, \mu_F^2) f_j(x_j, \mu_F^2)$$

$$\times \hat{\sigma}^{ij \to t\bar{t}}(\rho, m_{top}^2, x_i, x_j, \alpha_S(\mu_F^2), \mu_F^2, \mu_R^2) \quad (3.1)$$

Here $f_i(x_i, \mu_F^2)$ and $f_j(x_j, \mu_F^2)$ are the PDFs of the two protons, $\rho = 4m_{top}^2/\sqrt{\hat{s}}$ and $\hat{s} = x_i x_j s$ is the center-of-mass energy squared of the parton interaction. The indices i and j run over all $q\bar{q}$, gg, qg and $\bar{q}g$ pairs. μ_F is a theoretical scale used within perturbative QCD to extract the PDFs. The theoretical scale μ_R is introduced in the renormalization procedure of the perturbative QCD. In principle the total cross section $\sigma^{t\bar{t}}(\sqrt{s}, m_{top})$ should be independent of both scales μ_F and μ_R when going to infinite order of perturbation theory. The dependence of a theoretical calculation on the variation of these scales in taken as a measure of the precision in the calculation.
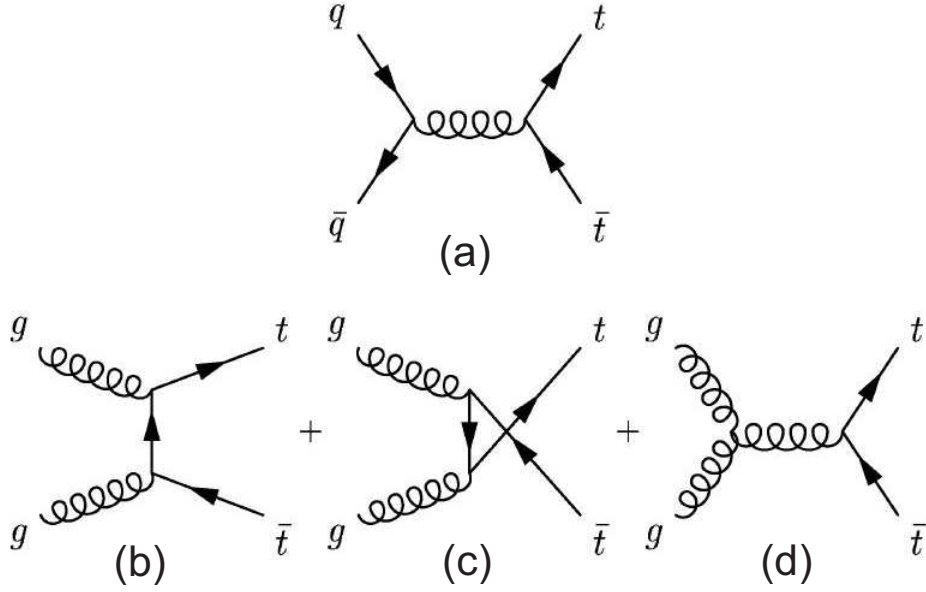
Figure 3.3: Lowest order Feynman diagrams for $t\bar{t}$ production at hadron colliders [5].

In Figure 3.3 the lowest order Feynman diagrams for $t\bar{t}$ production from two partons are shown. In principle, there are two channels for $t\bar{t}$ production: production from a quark-antiquark pair (a) and production from two gluons (b-d). At the LHC the ratio of these channels is roughly 1 : 9. The reason lies in the high center of mass energy at the LHC and the structure of the PDFs. For the production of two top quarks with $m_{top} \approx 170$ GeV the center-of-mass energy of the parton interaction has to be at least $\hat{s} \geq 4m_{top}^2 \approx 340^2$ GeV^2. With a center-of-mass energy of $s = 1.4$ TeV one gets $x_1 x_2 \geq 4m_{top}^2/s \approx 0.024^2$. A comparison of this value with the PDFs shows that the gluon-gluon channel clearly dominates at the LHC.

3.2 The Decay of the Top Quark

Besides its high mass, the top quark has another property which makes it special within all quarks. Its lifetime is expected about 4×10^{-25} s which is lower than the typical formation time for hadrons $1/\Lambda_{QCD} = 2 \times 10^{-24}$ s. As a consequence the top quark does not form hadrons before it decays. Further more, the spin information of top quarks is transmitted to the decay products and is thus accessible experimentally.

The top quark typically decays into a b quark and a W boson. Decays into d and s quarks are suppressed by their squared CKM matrix elements $|V_{td}|^2$ and $|V_{ts}|^2$. If the CKM matrix is assumed to be unitary the value of V_{tb} is $0.999100^{+0.000034}_{-0.000004}$ [3]. A combination of experimental results from CDF and DØ sets a lower limit of $|V_{tb}| > 0.78$ at 95% confidence level [3].

The W boson from the top decay further decays into a lepton- or quark-pair. According to the W decay one can group the decays of top-antitop pairs in different decay channels as shown in Figure 3.4. Top-antitop decays where both W bosons decay into a lepton and a neutrino are called dilepton channel. Decays where one W boson decays into leptons and the other W boson
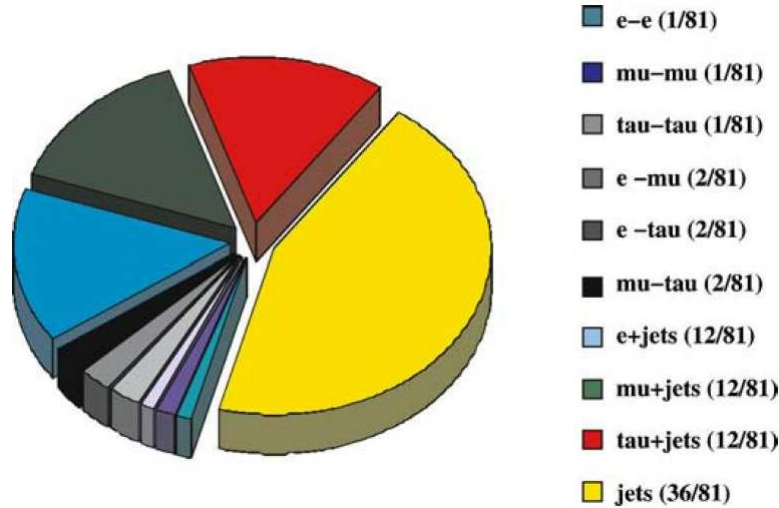
Figure 3.4: The top-antitop decay channels and their branching fractions in leading order calculation [5].

into quarks are called semileptonic channel. Decays into quarks only are called full hadronic channel. The ratio of the three decay channels in leading order calculation is 1:4:4.

The semileptonic channel is of special interest from the experimental point of view. While the dilepton channel suffers of its low branching fraction of 11% and two undetectable neutrinos in the final state, the full hadronic channel suffers a lepton in the final state that is needed for triggering and background reduction. The semileptonic channel is the best compromise with one lepton in its final state, a relatively high branching fraction of 44% and one neutrino in the final state which can be reconstructed from missing energy in the detector.

Because taus are difficult to identify in a detector often only semileptonic events with the W decaying into electrons or muons are regarded. These have a branching fraction of 29.6% .

3.3 The Top Quark Mass

Since the discovery of the top quark, the CDF and DØ experiments have carried out several direct experimental measurements of the top quark mass. The most recent world average value of $m_{top} = 170.9 \pm 1.1(\text{stat}) \pm 1.5(\text{syst})$ GeV [4] is a combination of different analysis methods applied in different decay channels from both experiments. The two main methods are the template method and the matrix element method.

In the template method the invariant mass of the 4-vector-sum of the decay products from the top quark is reconstructed. To determine the top quark mass, the invariant mass distribution of the top quark decay products is compared to Monte Carlo samples generated for different top quark masses. This approach has the advantage of being simple to compute. However it does not use all kinematic information of an event.

The matrix element method makes use of the fact that the cross section for top-antitop production depends on the top quark mass. The cross section calculated for an event with certain

kinematics can thus be used to estimate the probability to observe this event as a function of the top quark mass. The best value for the top quark mass is the mass that gives the highest product of probabilities for all events. In this approach in principle all kinematic information of an event can be used. However, for reasonable computing time simplifications have to be made.

Due to much higher statistics the LHC will allow measurements of the top quark mass with uncertainties close to 1 GeV [9]. At this precision uncertainties in the definition of the top quark mass become relevant. The kinematics of the top quark mass which is measured in experiments does not precisely correspond to the pole mass that appears in the perturbative top quark propagator. This ambiguity gives rise to a systematic uncertainty of order $\Lambda_{QCD} \sim$ 0.3 GeV.

In this work we investigate an alternative method to measure the top quark mass that aims to reduce the systematic uncertainty coming from the top quark mass definition. Instead of looking at the invariant mass of the top quark we will use a global (event shape) variable that characterizes top quark events, the invariant mass of the top-antitop quark system.

3.4 The Invariant Mass of the Top-Antitop Quark System

The invariant mass of the top-antitop quark system is given by

$$m_{t\bar{t}} = \sqrt{(E_t + E_{\bar{t}})^2 - (\vec{p}_t + \vec{p}_{\bar{t}})^2} \,, \tag{3.2}$$

where $\vec{p}_t$ and $\vec{p}_{\bar{t}}$ are the momenta of the top and the anti-top quark. In the leading-order s-channel production of $t\bar{t}$ pairs as shown in Figure 3.3 (a) and (d), $m_{t\bar{t}}$ corresponds to the invariant mass of the gluon that splits in the $t\bar{t}$ pair.

The cross section for $t\bar{t}$ production (see Equation (3.1)) can be expressed as a function of $m_{t\bar{t}}$. The differential cross section $\frac{d\sigma_{t\bar{t}}}{dm_{t\bar{t}}}$ will from here on be called the $m_{t\bar{t}}$ distribution. Figure 3.5 shows the $m_{t\bar{t}}$ distribution calculated in leading order (LO) and next-to-leading (NLO) order [10]. Another NLO calculation of the $m_{t\bar{t}}$ distribution can be found in Ref. [11].

The shape of the $m_{t\bar{t}}$ distribution can be understood as follows. The distribution is zero for $m_{t\bar{t}} < 2m_{top}$ since $2m_{top}$ is the minimum energy that is required for the production of a $t\bar{t}$ pair. The exponential decline at high $m_{t\bar{t}}$ can be explained in the following way. At leading order $m_{t\bar{t}}$ is equal to the center-of-mass energy of the parton interaction, $m_{t\bar{t}} = \sqrt{\hat{s}} = \sqrt{x_i x_j}\sqrt{s}$. High $m_{t\bar{t}}$ are thus suppressed by the gluon PDFs that steeply fall as a function of the momentum fraction x.

In Figure 3.5 one can see that the deviation of the shape of the $m_{t\bar{t}}$ distribution between LO and NLO calculation is within 5% . The higher order corrections to the LO distribution are thus small. Higher order corrections in Monte Carlo are typically of order 10-20% . Here small higher order corrections to the $m_{t\bar{t}}$ distribution thus motivate the use of this distribution for a top quark mass measurement.
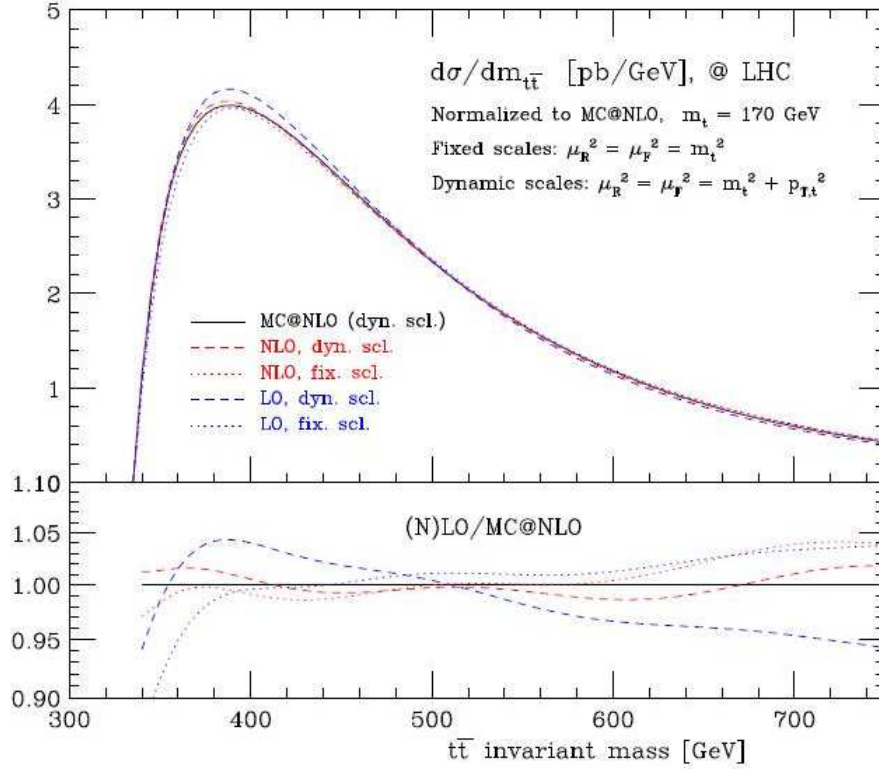
Figure 3.5: The $m_{t\bar{t}}$ distribution calculated at leading order (LO) and next-to-leading (NLO) order [10]. The distributions are normalized to the MC@NLO generator [12] cross section.

3.4.1 Top Quark Mass Information in the $m_{t\bar{t}}$ Distribution

The $m_{t\bar{t}}$ distribution strongly depends on the top quark mass. On the one hand, the cross section for $t\bar{t}$ production which determines the normalization of the $m_{t\bar{t}}$ distribution, strongly depends on the top quark mass. On the other hand, the shape on the $m_{t\bar{t}}$ distribution changes with the top quark mass. This is clear from the fact that the lower edge of the $m_{t\bar{t}}$ distribution is given by $2m_{top}$. From the experimental point of view the change of the shape is of more interest than the cross section change since cross section measurements involve high systematics uncertainties from the luminosity measurement.

To get a quantitative idea of the correlation of the shape of the $m_{t\bar{t}}$ distribution and the top quark mass, one can plot the mean of the $m_{t\bar{t}}$ distribution, $\langle m_{t\bar{t}} \rangle$, as a function of the top quark mass. This is demonstrated in Figure 3.6.

$\langle m_{t\bar{t}} \rangle$ and m_{top} show a strong correlation which is almost linear. Figure 3.6 also shows the theoretical uncertainties due to the scales μ_R and μ_F in the perturbative NLO calculations. The estimated relative theoretical uncertainty on the top quark mass is given by

$$\frac{\Delta m_{top}}{m_{top}} \sim 1.2 \frac{\Delta \langle m_{t\bar{t}} \rangle}{\langle m_{t\bar{t}} \rangle} + 0.005 \; . \tag{3.3}$$

If $\langle m_{t\bar{t}} \rangle$ could be measured with high accuracy, a top quark mass uncertainty of 0.5% due to scale uncertainties in theoretical calculations could be reached. Including more shape information from the $m_{t\bar{t}}$ distribution could even lead to better results. This indicates that the shape
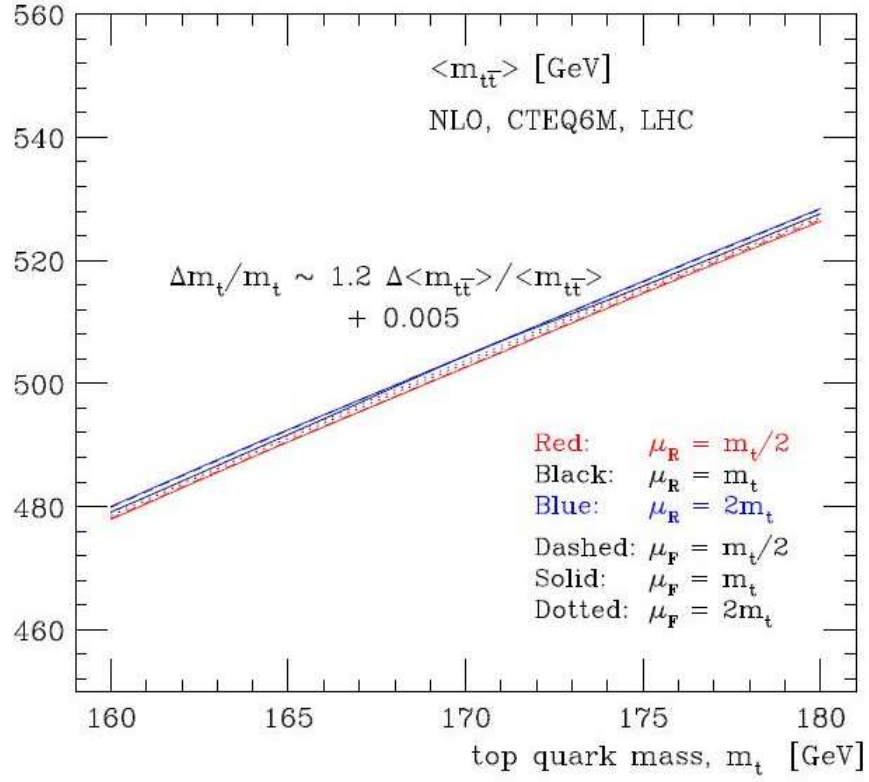
Figure 3.6: The mean of the $m_{t\bar{t}}$ distribution, $\langle m_{t\bar{t}} \rangle$, as a function of the top quark mass [10].

of the $m_{t\bar{t}}$ distribution from a theoretical point of view is a good variable for a top quark mass measurement.

4 Event Generators

The analysis of event data from particle colliders is a challenging process. To extract event information such as the top quark mass from data, a precise model of the expected event kinematics is needed. For this purpose Monte Carlo event generators are used. They simulate the event kinematics of the physics process of interest. The output of event generators is then typically given to detector simulation and reconstruction algorithms to get a good understanding of the kinematics of the physics process as seen in the detector.

The event generation is typically done in several steps. First, the process of interest is calculated at parton level (see Equation 3.1 for the $t\bar{t}$ cross section calculation). Second, hadronization of the partons and higher order effects are added to give a good description of what is observed in the detector. A brief description of these steps will be given in the following sections.

4.1 Event Generation at Parton Level

A typical parton level event generator which is currently used at the CMS experiment is ALPGEN v2.12 [13,14]. It can be used to calculate several hard scattering process at hadron colliders, including $t\bar{t}$ and W+jets production. These processes are calculated using the exact leading order (LO) evaluation of the partonic matrix element. The decay of top quarks and W bosons into quarks and leptons can also be computed.

In addition to the calculation of the leading-order diagrams, ALPGEN is also able to perform calculations at tree level for processes with higher jet multiplicities such as $t\bar{t}$ plus up to 6 additional jets. This is of great importance for generation of Monte Carlo events for the LHC due to the very large rate of $t\bar{t}$ and W+jets events with high jet multiplicities.

4.2 Hadronization and Simulation of Higher Order Effects

With parton level event generators such as ALPGEN computation of the hadronization of the generated partons is not possible. For this purpose the generated events are handed over to a general-purpose generator. At the CMS experiment PYTHIA v6.409 [15] is currently used. PYTHIA computes hadronization as well as several higher order effects needed for a good description of what is seen in the detectors at hadron colliders which are listed in the following.

- *Parton shower, initial and final state emission:* The parton shower algorithm simulates the emission of additional partons from the generated partons before hadrons are build. Both initial as well as final state emissions are simulated.

- In the *hadronization* the partons are turned into colorless hadrons. Since hadronization cannot be calculated in perturbative QCD, it is performed using a phenomenological model based on the so-called 'String Model'.

- *Multiple parton-parton interactions* can happen in addition to the hard interaction, between partons of the two proton remnants.

- *Multiple proton interactions* can occur when more than one proton-proton interaction takes place during one bunch crossing.

- The *underlying event* describes the energy flow beyond the energy resulting from the hard interaction.

4.3 Jet-Parton Matching

By combination of several multi-jet samples from ALPGEN (e.g. $t\bar{t}$+0,1,2,3,4 jets) a good description of additional jets can be reached. The use of PYTHIA for showering supports a good description of soft radiation. A combination of both approaches is thus desirable. However, this combination has to be done with care since both approaches overlap.
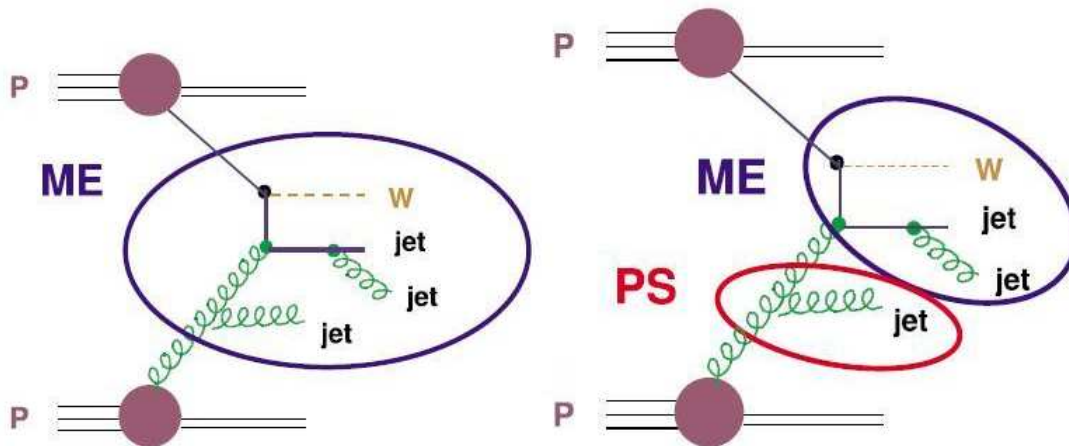
Figure 4.1: Tree level diagram for W+3jets and for W+2jets with one jet from parton shower [5].

Figure 4.1 shows the tree level diagram for W+3jets and for W+2jets with one jet from parton shower. Even though the diagrams are from different samples they can have the same kinematics. Combination of both samples will thus lead to double counting of events with certain kinematics.

This can be avoided by so called jet-parton matching. ALPGEN provides the MLM matching algorithm named after Michelangelo L. Mangano [16]. In this algorithm the matrix element

partons are matched to parton jets after showering. To avoid the double counting, all events with not matched matrix element partons or parton jets are rejected. In the sample with highest jet multiplicity additional jets from showering are allowed. In this procedure the actual definition of a jet (e.g. minimum p_T) decides which radiation is treated as hard (from multi-jet sample) or soft (from parton shower). Typically a p_T-cut decides which jets are described by the multi-jet samples and by the showering.

5 The LHC Accelerator and the CMS Experiment

5.1 The Large Hadron Collider

The Large Hadron Collider (LHC) is a proton-proton collider which is currently being constructed at the Conseil Européen pour la Recherche Nuclèaire (CERN) [5,17]. It is built in the tunnel of the former Large Electron-Positron Collider (LEP) with a circumference of 27 km. The LHC is designed to accelerate two proton beams to an energy of 7 GeV each, resulting in a center-of-mass energy of up to $\sqrt{s} = 14$ TeV. Its design luminosity is $\mathcal{L} = 10^{34}$ cm^{-2}s^{-1}. In addition to proton-proton collisions the LHC is also designed for heavy ion collisions (e.g. Pb-Pb) with $\sqrt{s} = 5.5$ TeV and $\mathcal{L} = 10^{27}$ cm^{-2}s^{-1}.

The colliding particles are accelerated in two separated beam pipes that have crossing points for collisions at four detector sites. The particle beams are kept on track by high-field superconducting NbTi dipole magnets which can produce magnetic fields of up to 8.3 T. They need to be cooled down to 1.9 K to reach their superconducting phase. For this purpose both beam pipes are included in a shared cryostatic system.

Figure 5.1 shows the accelerator and detector facilities at CERN. To reach energies of 7 TeV, the particles run through a chain of accelerators. Protons from a hydrogen source are first accelerated by the Linac to energies of 50 MeV. In the Booster, PS and SPS their energy is then increased sequentially to 1.4 GeV, 25 GeV and 450 GeV. Finally they are accelerated up to 7 TeV in the LHC. After acceleration the protons will move through the LHC in bunches of 10^{11} protons with an average length of 7.5 cm and a bunch spacing of 25 ns. This corresponds to the design luminosity of 10^{34} cm^{-2}s^{-1}. During the first two years of operation, it is, however, planned to run at a lower luminosity of up to 2×10^{33} cm^{-2}s^{-1}.

At four points of the accelerator ring protons can be brought to collision. Four different experiments are being constructed at these points as shown in Figure 5.1. The ATLAS (A Toroidal LHC ApparatuS) and CMS (Compact Muon Solenoid) experiments are general-purpose detectors which cover a wide range of physics analyses. ALICE (A Large Ion Collider Experiment) is especially constructed for the investigation of heavy ion collisions. LHC-b (Large Hadron Collider beauty Experiment) aims to analyze phenomena in decays of B-mesons with high precision and high statistics.

CERN Accelerators
(not to scale)

CMS

LHC

COMPASS

North Area

SPS

ALICE

T18

LHC-b

ATLAS

T12

West Area

*neutrinos

ISOLDE

CNGS

East Area

T10

AD

*pbar

PSB

E1

PS

TT2

E0

E2

LINAC2

LINAC3

LEIR

protons
antiprotons
ions
neutrinos to Gran Sasso (I)

p   Pb ions

Gran Sasso (I)
730 km

LHC: Large Hadron Collider
SPS: Super Proton Synchrotron
AD: Antiproton Decelerator
ISOLDE: Isotope Separator OnLine DEvice
PSB: Proton Synchrotron Booster
PS: Proton Synchrotron
LINAC: LINear ACcelerator
LEIR: Low Energy Ion Ring
CNGS: Cern Neutrinos to Gran Sasso

Rudolf LEY, PS Division, CERN, 02.09.96
Revised and adapted by Antonella Del Rosso, ETT Div.,
in collaboration with B. Desforges, SL Div., and
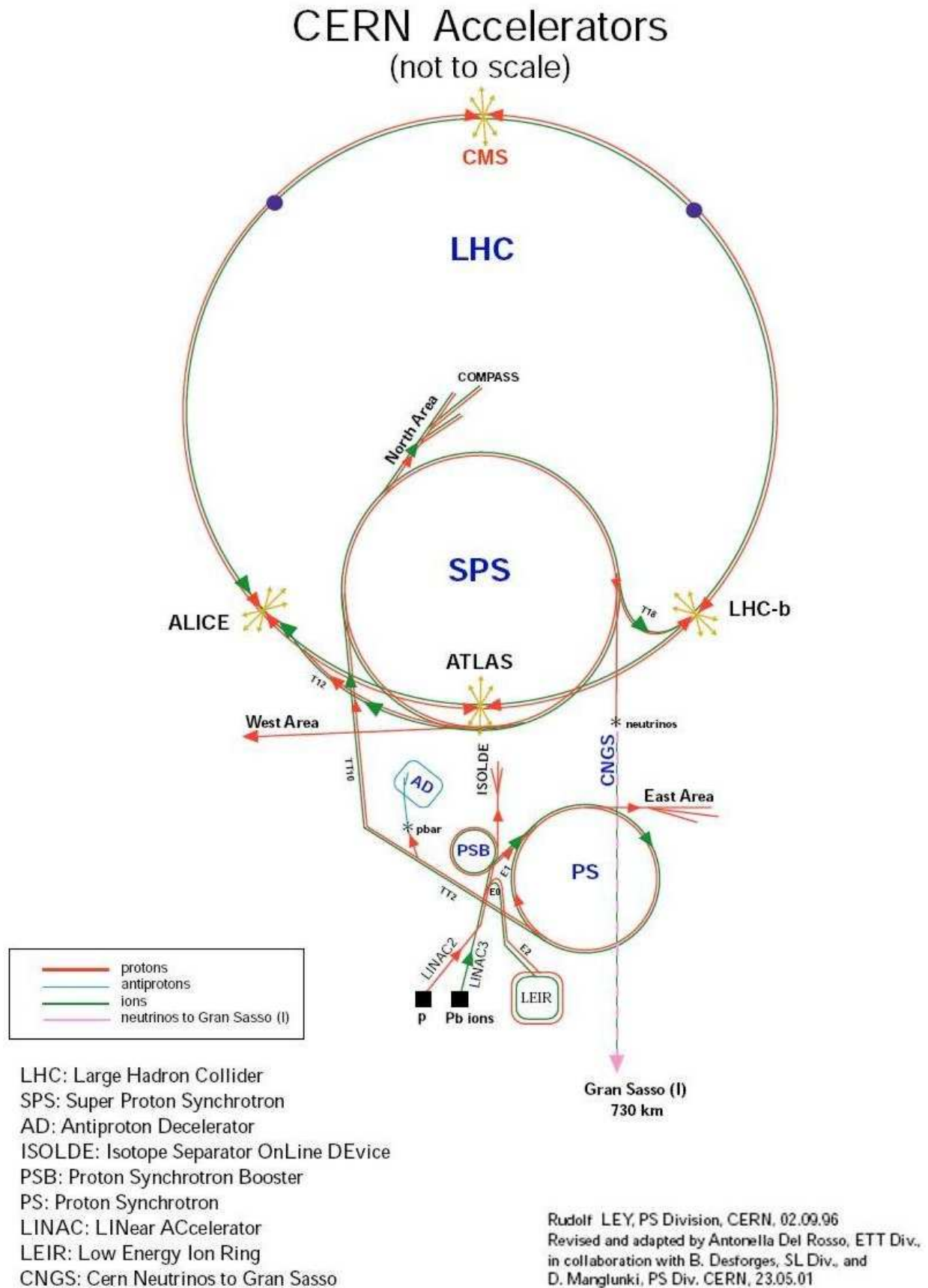D. Manglunki, PS Div. CERN, 23.05.01

Figure 5.1: The accelerators and detectors at CERN [18].

5.2 The CMS Detector

The CMS detector is designed for the search of the Higgs boson and new physics as well as for precision tests of the Standard Model [5,17,19]. For this purpose it has to be able to detect and identify several different kinds of particles including leptons, photons and jets. This implies several design goals for the CMS detector. Particularly, the CMS detector should allow good identification of charged particles (e.g. electrons, muons) as well as a precise measurement of their momenta. Also a high precision measurement of their tracks is required for the reconstruction of secondary vertices that is needed for identification of jets originating from b quarks. These goals are achieved by the design presented in the following.
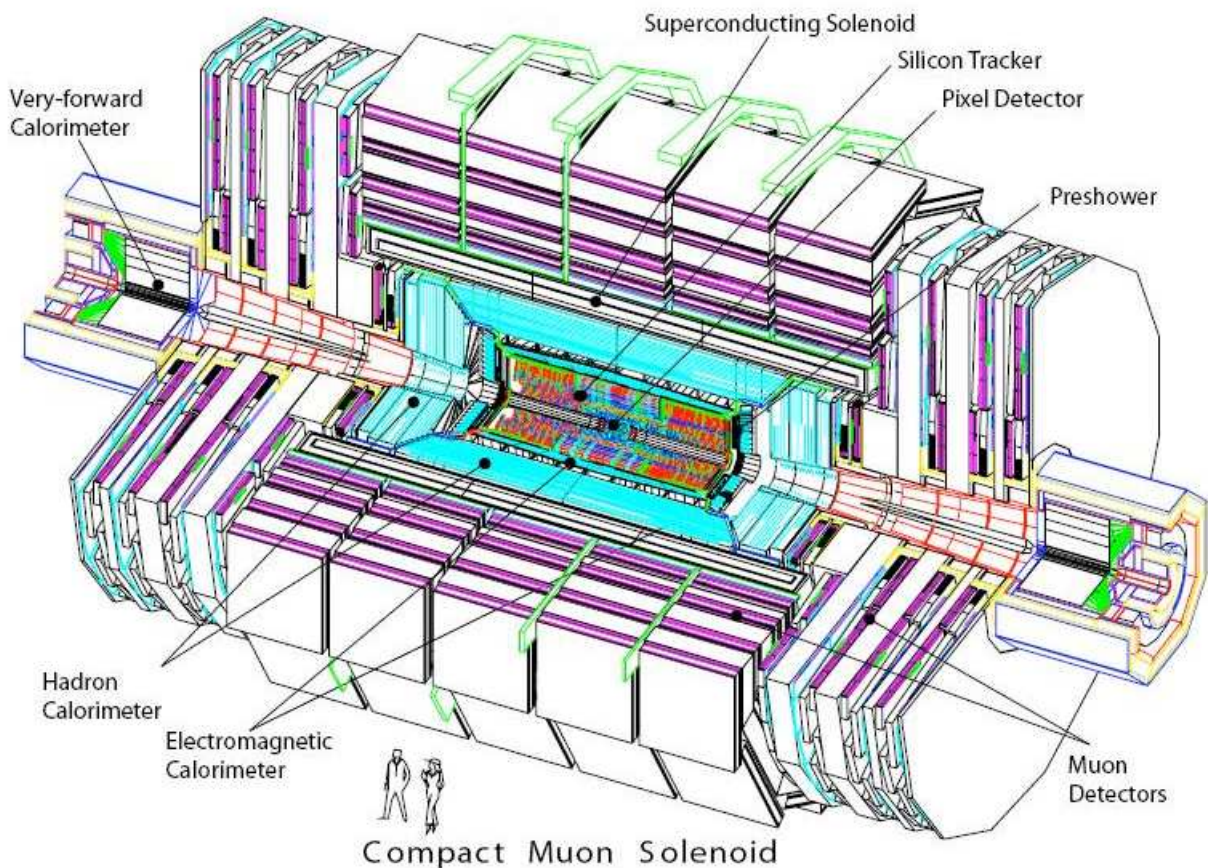
Figure 5.2: Cutaway view of the CMS detector and its compounds [17].

Figure 5.2 shows a cutaway view of the CMS detector and its compounds. The CMS detector has a diameter of 15 m, is 21.6 m long and weighs about 12500 t. It surrounds the collision point in its center to detect as many particles as possible that are produced in the proton-proton collisions. Several sub-detectors are organized in a barrel part and two forward parts. From the center outwards the CMS detector consists of the following compounds.

- The *Pixel Detector* and the *Silicon Tracker* together form the *Tracker* that provides information on particles' momenta and vertices.

- The *Electromagnetic Calorimeter*, the *Preshower Detector*, the *Hadronic Calorimeter* and the *Very Forward Calorimeter* provide information on particle energies and directions.

- The *Superconducting Solenoid* can generate a magnetic field of up to 4 T in the central part of the detector to enable determination of particle momenta from their tracks. The magnet is surrounded by several return yokes made of iron that return the magnetic field of the solenoid. They shape the magnetic field outside of the solenoid to enable determination of particle momenta also in the *Muon System*.

- The detectors of the *Muon System* are installed in the return yokes of the magnet and provide identification of muons and measurement of their momenta.

For the description of the CMS detector the following coordinate system is used. The origin is set to the center of the detector. The z-axis is chosen parallel to the beam axis. The x-axis lies in the horizontal plane. Coordinates are then typically given by the z-component, the azimuthal angle ϕ measured in the x-y-plane from the x-axis and the pseudorapidity $\eta = -\ln\tan(\theta/2)$ where θ is the polar angle measured from the z-axis.

In the following three sections an overview over the main components of the CMS detector that are important for this analysis will be given. This is followed by a section on the triggering system of the CMS experiment.

5.2.1 The Tracker

The *Tracker* is required to measure particle tracks with high precision and provide vertex information for both the identification of the primary vertex of a collision and the identification of jets originating from b quarks, the so-called b-tagging. For this purpose it is built in the region closest to the beam pipe, from a radius of 4 cm to 115 cm. In this region it has to deal with high particle fluxes. The components of the *Tracker* need to be radiation hard and provide a measurement with high granularity in order to distinguish neighboring particle tracks. The technology chosen for this purpose at CMS are silicon detectors. To ensure radiation hardness, the *Tracker* needs to be cooled down to -10 °C. With more than 200 m^2 of silicon it is the largest detector of its kind.
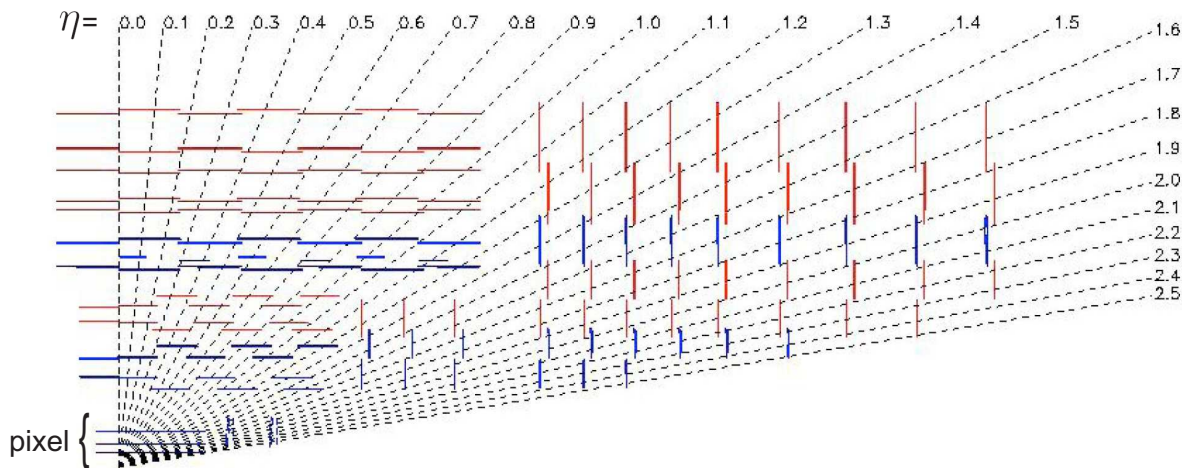

Figure 5.3: Layout of the tracker of the CMS experiment (1/4 of the z view) [17].

Figure 5.3 shows the layout of the *Tracker*. It consists of two main compounds that use different detection technology, the *Pixel Detector* and the *Silicon Tracker*.

The inner part of the *Tracker* up to a radius of 11 cm, the *Pixel Detector*, is built from three layers of silicon pixel detectors in the barrel and two layers in the endcaps. The pixels have a size of $100 \times 150 \ \mu m^2$ and give three dimensional information of particle tracks. The *Pixel Detector* is the essential part of the detector for the identification of vertices.

The outer part of the *Tracker*, the *Silicon Tracker*, consists of several layers of silicon strip detectors with strip widths of 80 μm (20 cm$< r <$ 55 cm) to 180 μm ($r >$ 55 cm). The layers are arranged into two barrel layers and endcaps with different radii to provide a maximum number of detector layers over the whole η-range of the *Tracker*. The strips supply two dimensional information on the particle tracks. Three dimensional information is derived by combining barrel and endcap information. Additionally, stereo layers of silicon strips which are twisted by an angle of 100 mrad also supply three dimensional information.

Overall, the *Tracker* covers the region of $|\eta| < 2.5$ and has 5×10^7 readout channels. The 3-dimensional vertex resolution of the *Tracker* is expected to be 15 μm with an occupancy of less than 1% at highest luminosity. The momentum resolution reached by the *Tracker* is of the order

$$\frac{\Delta p_T}{p_T} \approx 0.01\% \times p_T/\text{GeV} \ . \tag{5.1}$$

5.2.2 The Calorimeter

The *Calorimeter* is required to measure particle energies and directions. It consists of two parts, the *Electromagnetic Calorimeter* (ECAL) and the *Hadronic Calorimeter* (HCAL). The ECAL aims at the measurement of photons and charged particles such as electrons. Both calorimeters are used for measuring jets and determine the missing transverse energy. Figure 5.4 shows the layout of the two calorimeters. In contrast to other multi-purpose detectors, the *Calorimeter* of the CMS experiment is located almost fully inside the magnet coil. This design minimizes energy loss of particles before entering the *Calorimeter*.

The ECAL consists of 61200 scintillating $PbWO_4$ crystals that provide excellent energy resolution, radiation hardness and scintillation speed. In the barrel region they are read out by silicon avalanche photodiodes (APDs) which can operate in high magnetic fields. In the endcaps vacuum phototriodes (VPTs) are used which are more radiation hard. The length of the crystals is 23 cm (22 cm) in the barrel (endcaps) which corresponds to 26 (25) radiation lengths. In the forward region particle identification is enhanced by an additional *Preshower Detector* in front of the calorimeter crystals. Overall, the ECAL covers an η-range of $|\eta| < 3.0$ and allows the measurement of particle energies in $|\eta| < 2.5$. The energy resolution is expected to be

$$\frac{\sigma_E}{E} = \frac{2.7\%}{\sqrt{E/\text{GeV}}} \oplus \frac{20\%}{E/\text{GeV}} \oplus 0.55\% \tag{5.2}$$

in the barrel and

$$\frac{\sigma_E}{E} = \frac{5.7\%}{\sqrt{E/\text{GeV}}} \oplus \frac{25\%}{E/\text{GeV}} \oplus 0.55\% \tag{5.3}$$
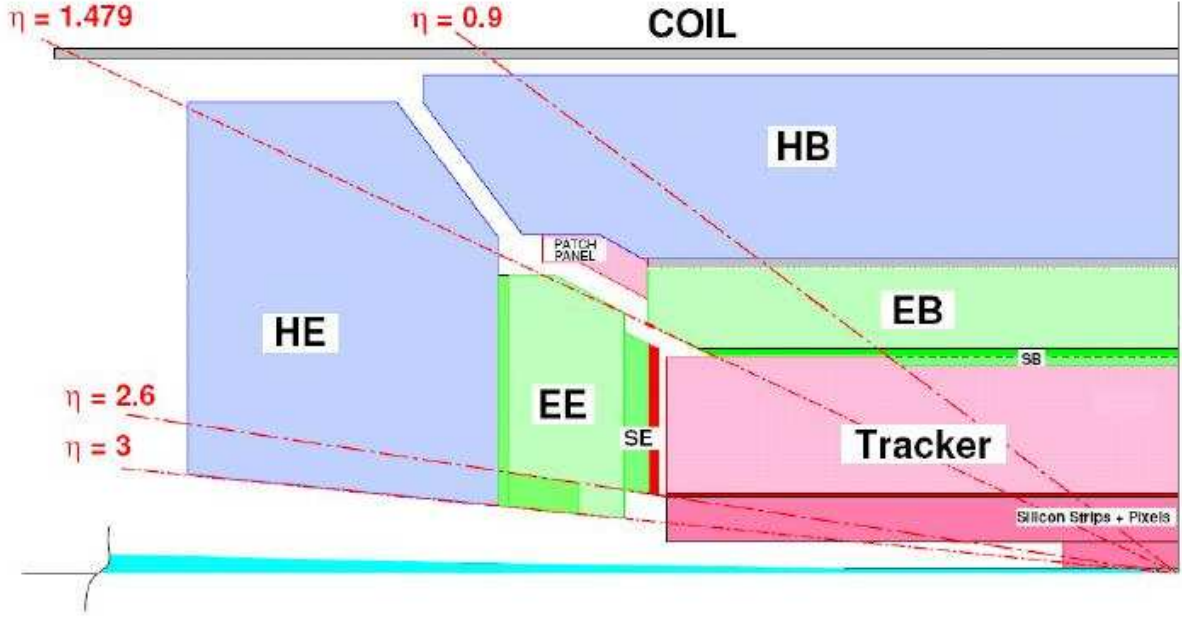
Figure 5.4: Layout of the calorimeters of the CMS experiment (1/4 of the z view) [17].

in the endcaps.

The HCAL consists of copper absorbers interleaved with plastic scintillators which are read out with wavelength-shifting fibers (WLS). In the barrel region the HCAL is extended by a tail catcher calorimeter outside the magnet coil to expand the depth of the HCAL to about 10 interaction lengths and support measurement of highly energetic jets. In the forward region the HCAL is extended by an iron/quartz-fiber calorimeter, the *Very Forward Calorimeter*, to allow detection up to $|\eta| < 5.0$, thus ensuring a comprehensive measurement of the missing transverse energy. The energy resolution is expected to be

$$\frac{\sigma_E}{E} = \frac{70\%}{\sqrt{E/\text{GeV}}} \oplus 9.5\% \tag{5.4}$$

in the barrel and

$$\frac{\sigma_E}{E} = \frac{127\%}{\sqrt{E/\text{GeV}}} \oplus 9\% \tag{5.5}$$

in the endcaps.

5.2.3 The Muon System

The *Muon System* is required to identify muons and measure their momenta and charge. It is located outside the calorimeters and the magnet. Since muons are the only charged particles that penetrate the *Calorimeter* and the magnet, tracks in the *Muon System* can be identified as muons. Figure 5.5 shows the layout of the *Muon System*.

The *Muon System* is integrated within the return yoke of the magnet which provides a magnetic field for momentum measurements. In the barrel region drift tubes (DTs) are installed. In
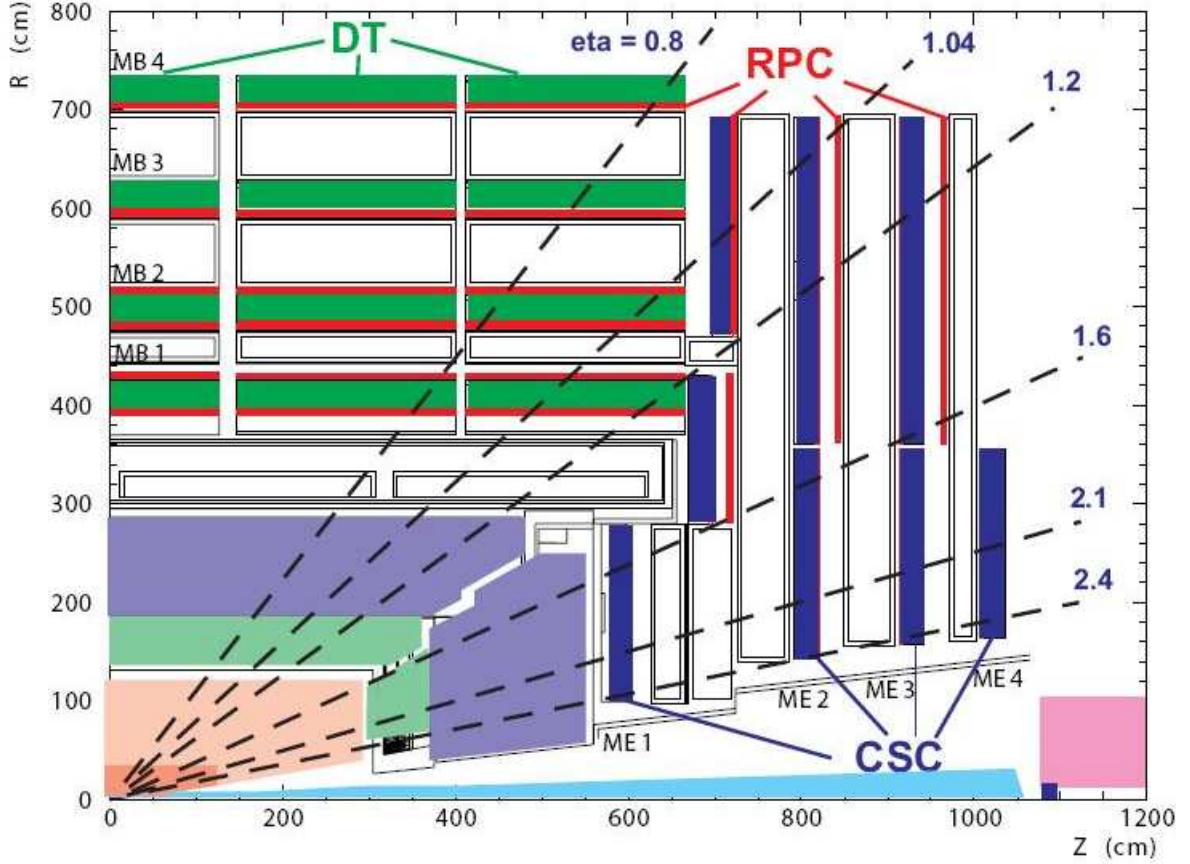
Figure 5.5: Layout of the muon system of the CMS experiment (1/4 of the z view) [17].

the forward region cathode strip chambers (CSCs) are used instead because of their good per-formance in strong magnetic fields and high rates. Additionally, both barrel as well as forward region are equipped with resistive plate chambers (RPCs) which provide fast timing and are used for trigger purposes.

Overall, the *Muon System* covers the region of $|\eta| < 2.4$ and has about one million readout channels. Best momentum resolution is achieved by combining *Tracker* and *Muon System* in-formation. The global momentum resolution is strongly η-dependent. For $p_T < 100$ GeV (1 TeV) it is expected to be 6%-20% (15% -35%). At low p_T the resolution is mainly achieved by the *Tracker*, whereas at high p_T the *Muon System* sets in and improves the global resolution.

5.2.4 The Trigger System

At the design luminosity of 10^{34} cm^{-2}s^{-1}, on average about 25 collisions per bunch crossing are expected every 25 ns. With $\sim 10^8$ readout channels which corresponds to about 1 MB of data per event, the CMS detector is expected to produce about 100 TB of data per second. However, the data storage system can handle only ~ 100 MB/s. To reduce the data rate to this level, a two-level trigger system, which filters events of interest for physics, is used at the CMS experiment.

The Level-1 trigger (L1) consist of custom hardware processors. It uses information from the *Muon System* and the *Calorimeter* to construct simple 'trigger primitive' objects such as muons,

electrons/photons, jets and the sums of E_T and E_T^{miss}. Simple cuts are applied to these objects to limit the event rate to 100 kHz (50 kHz at startup).

The High-Level Trigger (HLT) is software-based and runs on farm of commercial processors. It consists of two parts, the Level-2 and Level-3 triggers. The Level-2 trigger uses objects with finer granularity and higher precision than the Level-1 trigger. Also track information is exploited using simple algorithms. The Level-2 trigger thereby reduces the event rate by a factor of 10. In the Level-3 trigger finally a full event reconstruction is performed and the event rate is reduced to 100 Hz.

The decisions of the HLT trigger are made according to the so-called trigger menu which consists of several paths which have different requirements to an event. Events that pass at least one trigger path are passed on to the data storage system.

6 Detector Simulation, Event Reconstruction and Analysis Software

6.1 Detector Simulation

For a detailed understanding on how interactions in proton-proton collisions at the LHC are observed by the CMS detector, a dedicated simulation of the whole detector and the subatomic interactions is needed [17]. This simulation needs to simulate both the propagation of particles through the detector material as well as the response of the active detector components and their digital output.

The input to the detector simulation are collections of particles produced by Monte Carlo generators (see Chapter 4). The output is the digital signal from all detector components in the same format that is used for real data (RAW).

CMS uses two different software packages for detector simulation, the *Full Simulation* that describes the detector in full detail and the *Fast Simulation* which uses a parametrized response of the detector but has the advantage of being computationally fast to process. Both packages will be described in the following two sections.

6.1.1 Full Simulation

The *Full Simulation* of CMS uses the GEANT4 [20] toolkit. It allows modeling of the full detector geometry and the simulation of particles' propagation through magnetic fields as well as electromagnetic and hadronic interactions with the crossed material.

The *Full Simulation* is performed in two steps, the simulation step and the digitization step. In the simulation step particles are propagated through the detector allowing for interaction with detector material. Hits are produced on interaction with sensitive detector components. In the digitization step the electronic readout of these hits is simulated, taking into account resolution and detector response effects.

Another important feature of the detector simulation of CMS is the treatment of Pile-Up. Due to the high luminosity of the LHC, collisions from different bunch crossings may interact with the detector at the same time. In the detector simulation this effect can be taken into account by merging several collisions after their simulation step. However, in this analysis the simulation of Pile-Up was not used.

6.1.2 Fast Simulation

The *Fast Simulation* is designed to perform detector simulation with an accuracy comparable to the *Full Simulation* at a three orders of magnitude higher speed. The interactions simulated by the *Fast Simulation* are electron Bremsstrahlung, photon conversion, charged particle energy loss by ionization, charged particle multiple scattering and electron/photon/hadron showering.

In contrast to the *Full Simulation*, the simulation of hits and their digitization are not performed in two separate steps. Instead, the *Fast Simulation* directly produces high-level objects instead of hits, using parameterizations of resolutions and efficiencies of individual detector components. These high-level objects can be directly used as input to the reconstruction algorithms (see Section 6.2).

The major advantage of the *Fast Simulation* is its high computational speed of about one second per event which allows processing of huge amounts of Monte Carlo samples in a short time. Two example use cases for the *Fast Simulation* are the evaluation of systematic uncertainties and the production of samples with varying Monte Carlo generator parameters such as the top quark mass.

One should note that the *Fast Simulation* cannot entirely replace the *Full simulation* since it is tuned to the *Full Simulation*. Only the *Full Simulation* allows a detailed description of the interactions in the detector.

6.2 Event Reconstruction

The event reconstruction software of the CMS experiment has been designed to allow its use in both the offline reconstruction and the High-Level Trigger [17]. Reconstruction is first performed in each detector component locally. Step by step, different components are combined and the complexity of algorithms is increased.

In the following sections the reconstruction of the physics object relevant for this analysis will be described. These are muons, electrons, jets, the missing transverse energy and b-quark jets.

6.2.1 Muons

Muons are reconstructed using the *Muon System* and *Tracker* information in a three-step algorithm. First, a pattern-recognition algorithm is run in the *Muon System* to find seeds for the reconstruction of tracks. In a second step muon trajectories are constructed in the *Muon System* from the inside out using the Kalman-filter technique [21] and tracks are fitted. The result is a collection of muon tracks called *Standalone Muons*. In a third step these muon tracks are extrapolated to the *Tracker*. A track-reconstruction algorithm is run in the region of interest of the *Tracker* to obtain a collection of track candidates that correspond to the muon observed in the *Muon System*. The *Standalone Muon* and the track candidates are then combined and fitted

again. Finally, combinations that fulfill certain quality criteria are selected. The muon objects obtained in this way are so-called *Global Muons*.

The reconstruction efficiency for muons is more than 90% over almost the whole pseudo-rapidity range of $|\eta| < 2.4$. Typical resolutions for muons with $E_T = 20$ GeV are $\Delta E_T = 0.2$ GeV, $\Delta\phi = 3 \times 10^{-4}$ and $\Delta\eta = 4 \times 10^{-4}$. A detailed analysis of the E_T- and η-dependence of the resolution of all objects described in this chapter can be found in Ref. [22].

6.2.2 Electrons

Electrons are reconstructed using information from the *Electromagnetic Calorimeter* (ECAL) and the *Tracker* in three steps. In the first step energy deposits in the ECAL are combined to clusters (typically 3×3 crystals). To collect Bremsstrahlung radiated by the electrons before they reach the ECAL, so-called Superclusters are built from several clusters with the same η. The same η is required for the radiation because the electron motion is constrained by the magnetic field. The constructed Superclusters are then candidates for electrons. In a second step the *Pixel Detector* is searched for track hits corresponding to these Superclusters. Starting from these track hits, tracks a reconstructed in the whole *Tracker* using a Gaussian Sum Filter (GSF) [23]. In a third step tracks and Superclusters are combined and fitted. If the combinations of tracks and Superclusters fulfill certain quality requirements, they are identified as so-called *Pixel Match GSF Electrons*.

To distinguish electrons from jets the ratio of the energy deposited in the *Hadronic Calorimeter* (HCAL) tower just behind the electromagnetic cluster over the energy of the cluster H/E is calculated. The so-called electron ID requires $H/E < 0.2$ and other quality measures to define a sufficiently well measured electron candidate.

The reconstruction efficiency for electrons is typically more than 90% depending on the quality requirements. Typical resolutions for electrons with $E_T = 20$ GeV are $\Delta E_T = 0.5$ GeV, $\Delta\phi = 5 \times 10^{-4}$ and $\Delta\eta = 4 \times 10^{-4}$.

6.2.3 Jets

Partons produced in hard scattering QCD processes form particle jets in their hadronization. These jets typically deposit most of their energy in the *Calorimeter* in a cone of small size. The jet reconstruction starts with the combination of the cells of the ECAL and HCAL to so-called towers. These are then combined to jets using a jet algorithm.

There are two main types of jet algorithms, cone-algorithms and k_T-based algorithms [24]. In principle these algorithms can be applied to calorimeter towers as well as tracks or particles. In the following the *Iterative Cone Algorithm* which is used in this analysis will be described.

The *Iterative Cone Algorithm* starts form a list of objects ordered in E_T. A cone of size R is constructed around the object with highest E_T. All objects in this cone are then combined to a so-called proto-jet using $E_T = \sum_i E_{T,i}$, $\eta = \sum_i \eta_i E_{T,i}$, $\phi = \sum_i \phi_i E_{T,i}$. The direction of the

proto-jet is then used to construct a new cone. This procedure is repeated until the energy and direction changes per iteration are small (ΔE_T <1% , $\Delta R < 0.01$). All objects contained in the jet cone are then removed from the list and the next object with highest E_T is used as a seed for the next jet. This is repeated until all objects with a certain minimum E_T are removed from the list.

Typical resolutions for jets with $E_T = 50$ GeV are $\Delta E_T = 10$ GeV, $\Delta\phi = 0.08$ and $\Delta\eta = 0.06$.

The energy of the jets reconstructed from calorimeter towers usually differs from the energy of their original parton. This is due to particles from the parton decay that are not collected within the cone, Pile-Up, invisible particles in the jet and detector effects. Therefore a complex calibration of jet energies is needed [25]. Successively, corrections to the offset, η-dependence and p_T-dependence of the jet energy are applied. Finally a calibration of the absolute scale, the so-called Jet Energy Scale (JES), has to be performed.

The JES can in principle be determined using Monte Carlo information. However, to reduce the dependence of analyses on the accuracy of the Monte Carlo generators and detector simulation, data driven methods will be used as soon as data are available.

Two methods studied at CMS are the calibration from γ+jet events, and from $t\bar{t}$ events. The γ+jet method makes use of the fact that in leading order calculation of γ+jet production the p_T of the photon and the jet are equal. This approximately remains true also at higher orders. Since photon momenta are measured with high precision in the ECAL, γ+jet events allow a calibration of the jet energy. The jet energy calibration from $t\bar{t}$ events relies on the well known mass of the W boson. The mass constraint gives information on the energies of the two jets from the decay of the W.

6.2.4 Missing Transverse Energy

Imbalance of energy in the CMS detector provides information on invisible particles. Since particles escaping through the beam pipe cannot be measured, only the transverse component of the energy imbalance contains useful information.

The Missing Transverse Energy ($\not{E}_T$) is the transverse vector sum over all energy deposits in the *Calorimeter* [26]. Its components in x- and y-direction are given by

$$\not{E}_x = -\sum_i E_i \sin\theta_i \cos\phi_i \tag{6.1}$$

$$\not{E}_y = -\sum_i E_i \sin\theta_i \sin\phi_i . \tag{6.2}$$

Several corrections are applied to $\not{E}_T$. Muons deposit only a slight part of their energy in the *Calorimeter*. The $\not{E}_T$ is thus corrected by adding the transverse energies of the detected muons. Another important correction comes from the JES. The jet calibration is taken into account in $\not{E}_T$ by subtracting the difference between the transverse momenta of the corrected and the raw jets ($\vec{\not{E}}_T^{corr} = \vec{\not{E}}_T - \sum_i \vec{p}_i^{corr} - \vec{p}_i^{raw}$).

Typical resolutions for $\not{E}_T$ with $\not{E}_T = 50$ GeV are $\Delta E_T = 18$ GeV and $\Delta\phi = 0.8$.

6.2.5 B-Quark Jets

Many analyses require the identification of jets coming from b quarks. Jets from b quarks can be distinguished from light quark jets because they contain in average more charged particles and because of the lifetime of B hadrons of ~ 1.6 ps. Using these properties certain discriminators for b-jet identification, so-called b-tags, can be defined.
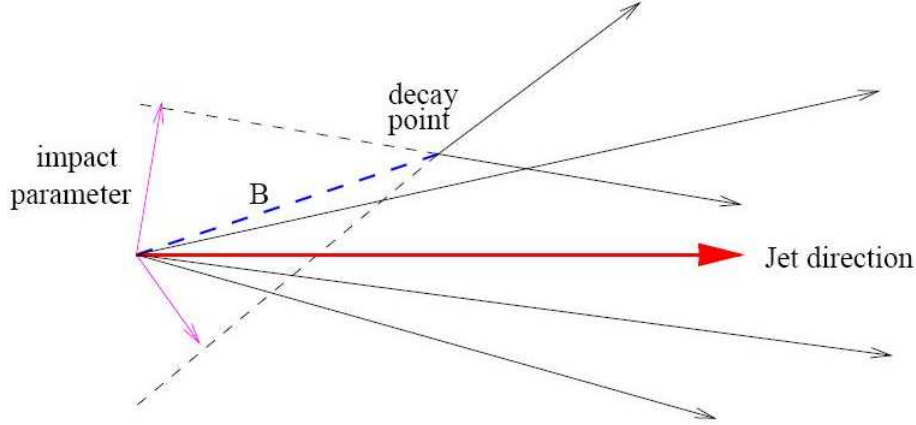

Figure 6.1: Representation (not to scale) of a hadronic jet originating from a b quark [27].

There are two common approaches to make use of the lifetime information. One approach is to reconstruct the secondary vertex of the B hadron decay. The second approach is to use an impact parameter as indicated in Figure 6.1. The impact parameters of tracks coming from particles from secondary vertices are typically higher than those from the primary vertex.

In the following the so-called track counting algorithm which is based on the impact parameter approach will be described [27]. The algorithm selects all tracks in a cone of $\Delta R < 0.3$ around the jet axis. The impact parameter is calculated for tracks fulfilling certain quality requirements (among others a $\chi^2/dof < 10$ from the track fitting), and is divided by its experimental resolution to evaluate its significance. The discriminator of the track counting algorithm is then defined as the impact parameter significance of the nth track ordered by significance. Figure 6.2 shows the distribution of the impact parameter significance of the second track (IPS(2nd)).

By applying a cut on the b-tag discriminator, jets can be categorized in b and light quark jets. The efficiency for identifying a b jet is then given by the fraction of b-tagged b-jets and all b-jets. The probability for misidentification of light quark jets as b jets (mistag rate) is defined similarly. In principle both efficiencies can be derived from Monte Carlo predictions. An extraction from real data is however desirable to minimize the dependency of analyses on the detector simulation. In Ref. [28] a method for calibration of b-tag efficiencies from $t\bar{t}$ events can be found.

In this analysis a cut of IPS(2nd) > 2.3 is applied to the impact parameter significance of the second track. This cut is a rather loose requirement and corresponds to a b-tag efficiency of 70.5% and a mistag rate of 10.0% .
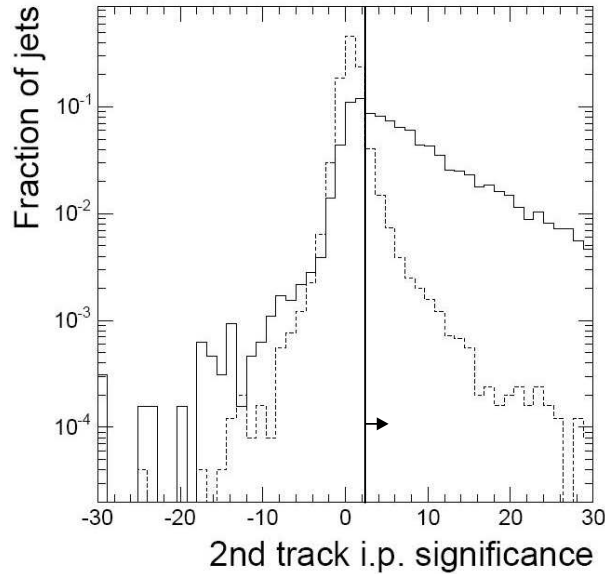
Figure 6.2: Impact parameter significance distribution for the second track ordered by significance. The solid line corresponds to the b-jet distribution while the dashed lines represent u, d, s and g jets. The vertical line and arrow indicate the cut applied in this analysis.

6.3 Analysis Software

The CMS collaboration has developed a software framework (CMSSW) that embodies software packages for all needs of analyses within the CMS experiment, such as event generation, detector simulation and event reconstruction. In this analysis the CMSSW framework is used for event generation (CMSSW_1_4_7) and detector simulation and event reconstruction (CMSSW_1_5_2 and CMSSW_1_6_7). The CMSSW versions 1_4_7, 1_5_2 and 1_6_7 are validated for their purposes used in this analysis and are consistent by design.

An additional package from the CMS top quark physics group, the Top Quark Analysis Framework (TQAF) [29], is used. It provides links to standard algorithms for particle identification as well as a commonly defined pre-selection of physics objects which will be described in Section 7.2.

For the analysis, the Physics eXtension Library (PXL) toolkit (version 1.0) [30] is used. The ROOT framework (version 5.13/04e) [31] is used for plotting of histograms.

7 Event Samples and Pre-Selection

7.1 The Event Samples

This section will give information on the Monte Carlo samples used in this analysis. The analysis makes use of the Monte Carlo samples for $t\bar{t}$ production as well as the main background process, W production with additional jets (W+jets). Other backgrounds, such as QCD multi-jet events, are not regarded but considered to be reducible with the cuts used in this analysis [32].

For the analysis concerning the reconstruction of $m_{t\bar{t}}$ (see Chapter 8), official samples are used. For the analysis concerning the top quark mass measurement from $m_{t\bar{t}}$ (see Chapter 9), additional private samples for $t\bar{t}$ production with different top quark masses are used.

All samples are generated with ALPGEN [13] combined with PYTHIA [15] to simulate higher order effects. Several ALPGEN samples with different jet-multiplicities are merged

Sample	Properties	Cross section [pb]	Number of generated events
W+0j		45000	100000
W+1j	$p_T(W) < 100\,\mathrm{GeV}$	9200	100000
W+1j	$100\,\mathrm{GeV} < p_T(W) < 300\,\mathrm{GeV}$	250	100000
W+2j	$p_T(W) < 100\,\mathrm{GeV}$	2500	99398
W+2j	$100\,\mathrm{GeV} < p_T(W) < 300\,\mathrm{GeV}$	225	99853
W+3j	$p_T(W) < 100\,\mathrm{GeV}$	590	58807
W+3j	$100\,\mathrm{GeV} < p_T(W) < 300\,\mathrm{GeV}$	100	100000
W+4j	$p_T(W) < 100\,\mathrm{GeV}$	125	100000
W+4j	$100\,\mathrm{GeV} < p_T(W) < 300\,\mathrm{GeV}$	40	49796
W+$\geq$5j	$p_T(W) < 100\,\mathrm{GeV}$	85	55579
W+$\geq$5j	$100\,\mathrm{GeV} < p_T(W) < 300\,\mathrm{GeV}$	40	43865
$t\bar{t}$+0j	$m_{top} = 175\,\mathrm{GeV}$	619	619000
$t\bar{t}$+1j	$m_{top} = 175\,\mathrm{GeV}$	176	176000
$t\bar{t}$+2j	$m_{top} = 175\,\mathrm{GeV}$	34	34000
$t\bar{t}$+3j	$m_{top} = 175\,\mathrm{GeV}$	6.0	6000
$t\bar{t}$+$\geq$4j	$m_{top} = 175\,\mathrm{GeV}$	1.5	1500

Table 7.1: Officially produced Monte Carlo samples for $t\bar{t}$ and W+jets production. The $t\bar{t}$ cross sections are next leading order cross sections obtained by applying a global next leading order to leading order k factor of 1.85 to the leading order calculation performed by ALPGEN [33].

Sample	Properties	Cross section [pb]	Number of generated events	
			Inclusive	Semileptonic only
$t\bar{t}$+0j	$m_{top} = 155$ GeV	1110	177298	137720
$t\bar{t}$+1j	$m_{top} = 155$ GeV	286	42817	39011
$t\bar{t}$+2j	$m_{top} = 155$ GeV	53	17458	13751
$t\bar{t}$+3j	$m_{top} = 155$ GeV	8.8	8634	5833
$t\bar{t}$+$\geq$4j	$m_{top} = 155$ GeV	2.4	448	1578
$t\bar{t}$+0j	$m_{top} = 165$ GeV	837	171691	136231
$t\bar{t}$+1j	$m_{top} = 165$ GeV	223	44061	39563
$t\bar{t}$+2j	$m_{top} = 165$ GeV	43	41379	24372
$t\bar{t}$+3j	$m_{top} = 165$ GeV	7.3	9154	6064
$t\bar{t}$+$\geq$4j	$m_{top} = 165$ GeV	1.9	343	369
$t\bar{t}$+0j	$m_{top} = 172$ GeV	673	167109	134196
$t\bar{t}$+1j	$m_{top} = 172$ GeV	191	52076	43122
$t\bar{t}$+2j	$m_{top} = 172$ GeV	39	52376	29255
$t\bar{t}$+3j	$m_{top} = 172$ GeV	6.1	9264	6113
$t\bar{t}$+$\geq$4j	$m_{top} = 172$ GeV	1.7	964	2428
$t\bar{t}$+0j	$m_{top} = 175$ GeV	618	167871	134535
$t\bar{t}$+1j	$m_{top} = 175$ GeV	177	55179	44499
$t\bar{t}$+2j	$m_{top} = 175$ GeV	37	45505	26204
$t\bar{t}$+3j	$m_{top} = 175$ GeV	6.1	8717	5870
$t\bar{t}$+$\geq$4j	$m_{top} = 175$ GeV	1.7	594	2264
$t\bar{t}$+0j	$m_{top} = 178$ GeV	591	166022	133714
$t\bar{t}$+1j	$m_{top} = 178$ GeV	163	55911	44824
$t\bar{t}$+2j	$m_{top} = 178$ GeV	32	16379	13272
$t\bar{t}$+3j	$m_{top} = 178$ GeV	5.7	8560	5801
$t\bar{t}$+$\geq$4j	$m_{top} = 178$ GeV	1.5	2586	3148
$t\bar{t}$+0j	$m_{top} = 185$ GeV	488	167969	134578
$t\bar{t}$+1j	$m_{top} = 185$ GeV	145	64677	48717
$t\bar{t}$+2j	$m_{top} = 185$ GeV	31	19528	14670
$t\bar{t}$+3j	$m_{top} = 185$ GeV	5.0	7613	5380
$t\bar{t}$+$\geq$4j	$m_{top} = 185$ GeV	1.3	2282	3013
$t\bar{t}$+0j	$m_{top} = 195$ GeV	363	170692	135787
$t\bar{t}$+1j	$m_{top} = 195$ GeV	112	65590	49122
$t\bar{t}$+2j	$m_{top} = 195$ GeV	24	18970	14423
$t\bar{t}$+3j	$m_{top} = 195$ GeV	4.0	6369	4828
$t\bar{t}$+$\geq$4j	$m_{top} = 195$ GeV	1.1	2279	3012

Table 7.2: Privately produced Monte Carlo samples for $t\bar{t}$ production with different top quark masses. Inclusive $t\bar{t}$ samples (third column) as well as semileptonic $t\bar{t}$ samples (fourth column) were produced. The next leading order $t\bar{t}$ cross sections were obtained analogously to the officially produced Monte Carlo samples in Table 7.1.

using the MLM-matching scheme [16] to provide a good description of physics events measured in the CMS experiment.

Table 7.1 summarizes the officially produced Monte Carlo samples for $t\bar{t}$ and W+jets production. They have been generated in CMSSW_1_4_7 in the *Summer07* production [33,34] and reconstructed using the *Full Simulation* and event reconstruction of CMSSW_1_5_2 in the (pre)*CSA07* computing exercise. In the MLM-matching (see Section 4.3) jets are required to have $p_T \geq 70$ GeV and $p_T \geq 20$ GeV for the $t\bar{t}$ and W+jets samples respectively.

Table 7.2 summarizes the privately produced Monte Carlo samples for $t\bar{t}$ production for different top quark masses. These samples are produced using the same procedure as the official $t\bar{t}$ samples in Table 7.1 except for the differences described in the following. The value of m_{top} is varied from 155 GeV to 195 GeV. A part of the production is constraint to the semileptonic channel to reduce computing time. The reconstruction is performed using the *Fast Simulation* and event reconstruction of CMSSW_1_6_7. With the *Fast Simulation* the production rate is about 20000 events per CPU-day.

7.2 The Pre-Selection

In the pre-selection several quality cuts are applied on the objects from the event reconstruction such as electrons, muons, jets and $\not{E}_T$ in oder to provide well defined physical objects for the analysis. The top quark analysis group has defined common pre-selections to allow easy comparison between analyses performed within the group [29,35]. In the following the standard pre-selection for semileptonic $t\bar{t}$ events will be described.

The *Global Muons*, the *Pixel Match GSF Electrons*, the *Iterative Cone Jets* with a cone size of $\Delta R < 0.5$ and the $\not{E}_T$ from the event reconstruction (see Section 6.2) are used as input for the pre-selection. The following cuts are applied to these objects,

- $p_T(\text{leptons}) > 20$ GeV , $\eta(\text{leptons}) < 2.4$,

- $p_T(\text{jets}) > 15$ GeV , $\eta(\text{jets}) < 2.4$.

In this analysis additional standard lepton isolation and identification criteria [35] are required as well,

- track isolation (muons) < 3 GeV , calorimeter isolation (muons) < 5 GeV ,

- track isolation (electrons) < 3 GeV , calorimeter isolation (electrons) < 6 GeV ,

- ID (electrons) $= 1$.

Isolation requirements are used in order to select leptons from the decay of a heavy boson (e.g. a W) and reject leptons originating from heavy quarks (e.g. b quarks) that form jets. Leptons from heavy quark jets typically have a high number of hits in both the *Tracker* and the *Calorimeter* in the region surrounding the lepton trajectory. An isolation criterion can thus be defined as the energy flow through a cone around the lepton with a size of $\Delta R = \sqrt{\Delta\eta^2 + \Delta\phi^2} < \Delta R_{max}$. The energy of the lepton itself is subtracted from this value. The energy flow can be constructed
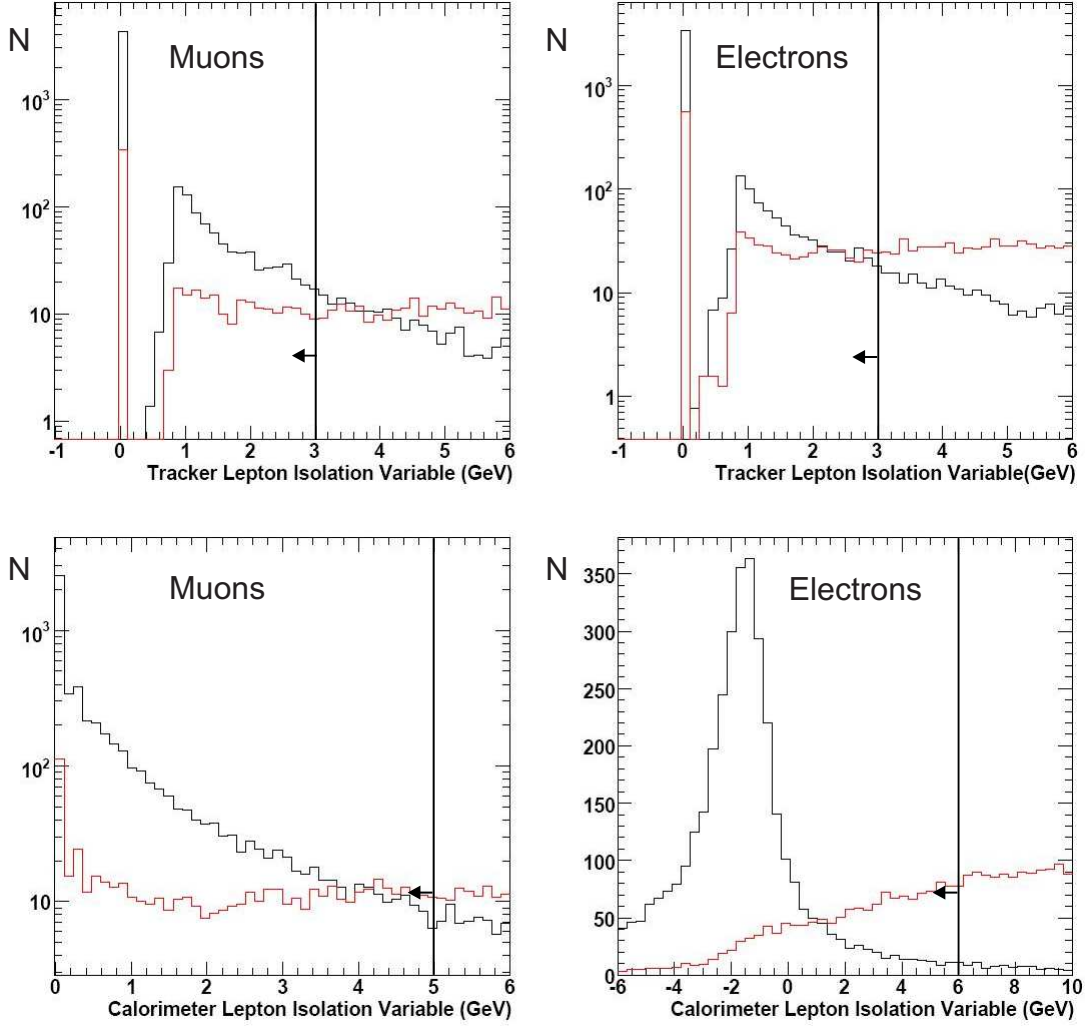
Figure 7.1: Distribution of the tracker and calorimeter isolation variables for muons (left) and electrons (right) in $t\bar{t}$ events [35]. The black histograms correspond to reconstructed leptons matched with leptons originating from the decay of a W boson, while the red histograms correspond to any other lepton defined using an angular matching criterion ($\Delta R < 0.15$). Vertical lines and arrows indicate the cuts applied in the pre-selection. Note that (a), (b) and (c) are shown using a logarithmic scale.

from the p_T of tracks (track isolation) in the *Tracker* or from the E_T of towers in the *Calorimeter* (calorimeter isolation).

The track isolation and calorimeter isolation variables are shown in Figure 7.1. In the determination of both track isolation and calorimeter isolation, a cone size of $\Delta R_{max} = 0.3$ is used. Note that a track isolation of 0 corresponds to a lepton that is surrounded by 0 tracks within a cone of size ΔR_{max}. Higher track isolation corresponds to the sum over p_T of all tracks within a cone of size ΔR_{max}.

Both isolation criteria provide a good handle on reconstruction quality, but also on background suppression. QCD multi-jet events, which typically do not contain isolated leptons, are expected to be strongly suppressed by isolation cuts.
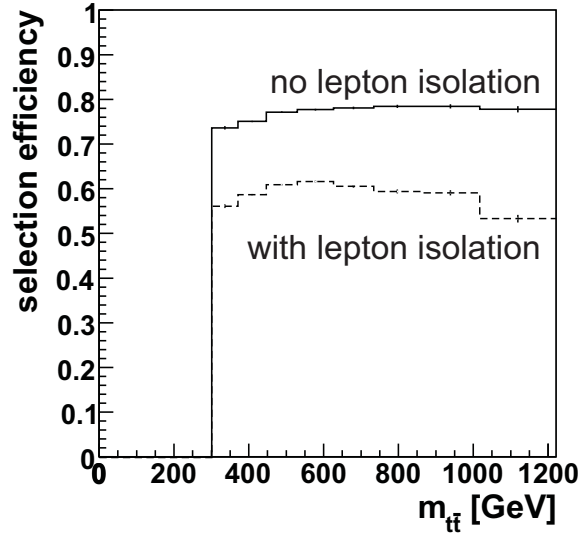
Figure 7.2: Selection efficiency of the pre-selection for semileptonic $t\bar{t}$ events as a function of $m_{t\bar{t}}$. The solid line corresponds to a pre-selection without lepton isolation and identification requirements, while the dashed line corresponds to the pre-selection with lepton isolation and identification requirements.

The pre-selection also imposes requirements on the event to reduce the analysis to a subsample of events that is enriched with semileptonic $t\bar{t}$ events. An event is required to have

- ≥ 1 lepton and ≥ 2 jets .

Figure 7.2 shows the selection efficiency of the pre-selection for semileptonic $t\bar{t}$ events as a function of $m_{t\bar{t}}$. In average 76.5% of all events pass the pre-selection without lepton isolation and identification requirements. The efficiency loss is mainly due to the limited detector acceptance of $|\eta| < 2.4$. With the requirement of lepton isolation and identification, the selection efficiency drops to an average of 59.7% .

As a function of $m_{t\bar{t}}$, the selection efficiency is almost flat up to $m_{t\bar{t}} = 1$ TeV. The impact due to the pre-selection on the shape of the $m_{t\bar{t}}$ distribution is thus expected to be small.

7.2.1 Trigger Efficiencies

When real data is taken, only events passing certain trigger paths of the L1 and HLT (see Section 5.2.4) are recorded. Not all events selected for the analysis from Monte Carlo samples actually pass a trigger path. To evaluate this effect, the efficiencies of several trigger paths are estimated for events which pass the pre-selection.

For the trigger study presented here [36], a slightly different pre-selection with no isolation and identification requirements for the leptons is used.

Table 7.3 summarizes the HLT trigger menu relevant for this analysis. Figure 7.3 shows the trigger efficiencies of these HLT paths for semileptonic $t\bar{t}$ events as a function of $m_{t\bar{t}}$. For this analysis the relevant region is $m_{t\bar{t}} < 1$ TeV. In this region the *Relaxed Electron* (Non Isolated)

HLT path	L1 threshold [GeV]	HLT threshold [GeV]	HLT rate [Hz]
Single Isolated μ	7	11	18.3
Single Relaxed μ	7	16	22.7
Single Isolated e	12	15	17.1
Single Relaxed e	15	17	9.6
E_T^{miss}	40	65	4.9
Single Jet	150	200	9.3

Table 7.3: Summary of the HLT trigger menu. Trigger rates are estimated for $\mathcal{L} = 10^{32}$ cm^{-2}s^{-1}. Isolated lepton triggers require the lepton to be isolated from jets, while relaxed lepton triggers do not require isolation.
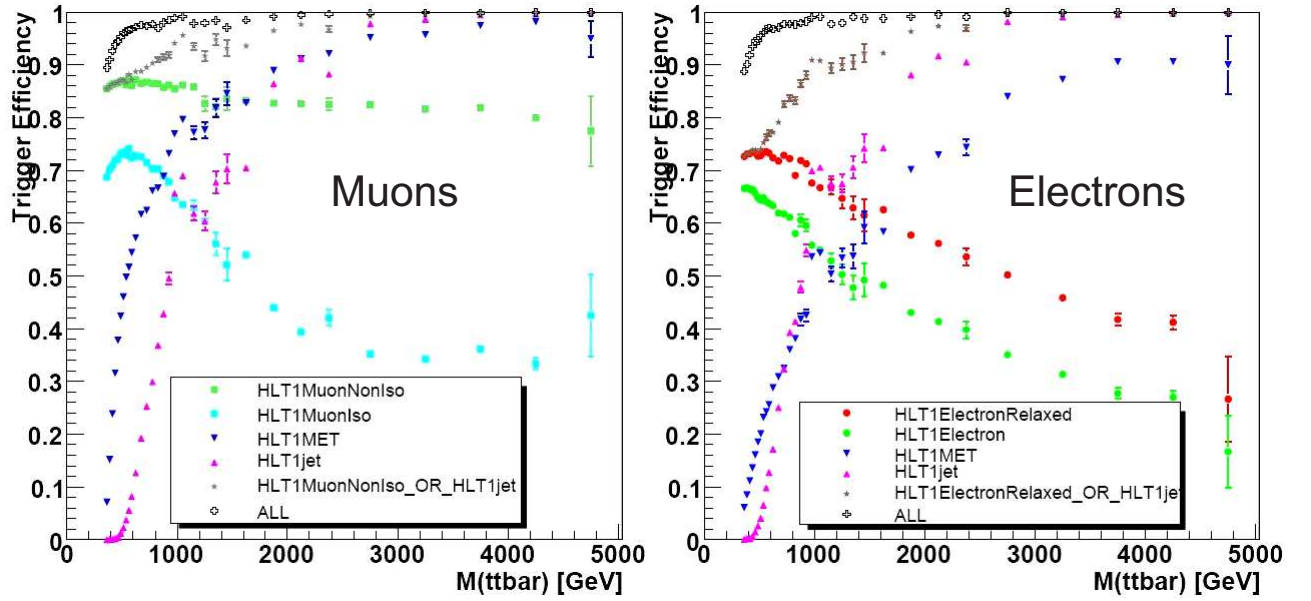
Figure 7.3: Trigger efficiencies after pre-selection of the most relevant HLT paths on semileptonic $t\bar{t}$ events in the muon (left) and electron (right) channel as a function of $m_{t\bar{t}}$ [36].

and the *Relaxed Muon* (Non Isolated) HLT triggers are sufficiently flat in $m_{t\bar{t}}$ and have efficiencies of about 73% and 86% , respectively. These triggers are thus good candidates for the use in this analysis. Due to the flatness of the evaluated trigger efficiencies as a function of $m_{t\bar{t}}$ the effect of trigger efficiency uncertainties is expected to have reasonably small impact on the shape of $m_{t\bar{t}}$. The analysis presented in the following will disregard trigger efficiencies.

In principle trigger efficiencies have to be estimated in detail for the final selection cuts of the analysis. The trigger efficiencies for the pre-selection can, however, be regarded as a lower limit of the efficiencies expected for the final (tougher) selection. It is expected that trigger efficiencies for the final selection that includes isolation cuts for the leptons will lead to higher trigger efficiencies. However, an analysis for confirmation needs to be performed.

8 Reconstruction of the Invariant Mass of the Top-Antitop Quark System

8.1 Reconstruction of m$_{t\bar{t}}$

This chapter gives a detailed description of the reconstruction of $m_{t\bar{t}}$ which will be used as input for the top quark mass measurement described in Chapter 9. The overall strategy will be outlined in the following.

The reconstruction of $m_{t\bar{t}}$ uses the semileptonic $t\bar{t}$ channel. This channel is chosen because of its low background contributions, unlike the hadronic channel, and the possibility to reconstruct all final state objects, unlike the dilepton channel with two neutrinos. Decays of the W bosons into taus are not regarded due to the difficulties involved in their reconstruction. In the following, non-semileptonic events and semileptonic events where one W boson decays into a tau will be called 'other $t\bar{t}$' events.
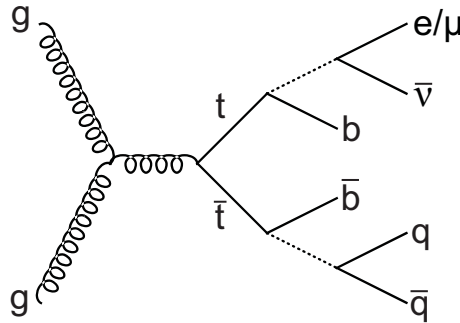
Figure 8.1: Example for a leading order Feynman diagram for semileptonic $t\bar{t}$ production.

Figure 8.1 shows one of the leading order Feynman diagrams for semileptonic $t\bar{t}$ production. In principle $m_{t\bar{t}}$ can be calculated by simply adding the 4-vector sum of all final state objects and building the invariant mass. This analysis however uses a more sophisticated approach. In order to improve the resolution of $m_{t\bar{t}}$, a kinematic fit is applied to the reconstructed objects to make use of well known information on the top quark decay.

The reconstruction is carried out in three steps for all events passing the pre-selection. First, possible event configurations are built. Second, a kinematic fit is applied to all configurations. And third, the best reconstructed configuration is selected. These three steps will be described in the following three sections.

8.1.1 Building Event Configurations

For a full reconstruction of both the top and the anti-top quark, four reconstructed jets, one lepton and $\not{E}_T$ are needed. In this analysis the four jets with highest p_T are selected as input to the reconstruction. Furthermore, the lepton (electron or muon) with highest p_T is selected. One should note that this selection does not always lead to a selection of the jets from the top quark decay if other high p_T jets are present in an event.

The momentum of the neutrino is reconstructed using $\not{E}_T$ and a W-mass constraint. The transverse momentum of the neutrino ($p_{\nu,T}$) is given by $\not{E}_T$ while the longitudinal momentum ($p_{\nu,L}$) of the neutrino is not measured in the detector. The longitudinal momentum is calculated using the fact that the neutrino comes from the decay of the W boson into a lepton and a neutrino. The fact that the invariant mass of the lepton-neutrino pair corresponds to the W boson mass M_W leads to a quadratic equation with up to two solutions. The neutrino momentum is given by

$$\vec{p}_\nu = \begin{pmatrix} \not{E}_x \\ \not{E}_y \\ \frac{1}{2p_{l,T}^2}(Ap_{l,L} \pm E_l\sqrt{A^2 - 4p_{l,T}^2 \not{E}_T^2}) \end{pmatrix} \tag{8.1}$$

with $A = M_W^2 + 2\vec{p}_{l,T} \; \vec{\not{E}}_T$ where $p_{l,T}$ ($p_{l,L}$) corresponds to the transverse (longitudinal) momentum of the lepton. There are two (one) possible solutions for the neutrino momentum if $A^2 - 4p_{l,T}^2 \not{E}_T^2 > 0$ (= 0). Otherwise Equation (8.1) gives imaginary solutions which can occur if $\not{E}_T$ is badly measured. In this case the neutrino momentum is set to the real part of the solution to allow reconstruction of all events. The neutrino solutions calculated in this way will be used as input values for the kinematic fit. The kinematic fit will recalculate the neutrino solution and is in principle able to find the right solution even for badly measured $\not{E}_T$.

For the reconstruction of the two top quarks, the selected four jets need to be assigned to their partons from which they originate. There are in principle 12 possible configurations if b-jets and light jets are regarded as indistinguishable. Taking into account the neutrino solutions, there are altogether up to 24 configurations. The requirement of one (two) identified b-jets reduces the maximum number of configurations to 12 (4).

Figure 8.2 (a) shows the number of configurations for semileptonic $t\bar{t}$ events that pass the preselection. Events with 2 identified b-jets have 1 or 2 configurations depending on the number of neutrino solutions. Events with 1 and 3 identified b-jets have 6 or 12 configurations. Events with 0 and 4 identified b-jets have 12 or 24 configurations. About one third of all events have only 1 neutrino solution, which is due to badly measured $\not{E}_T$, leading to 1, 6, and 12 configurations respectively.

In principle $m_{t\bar{t}}$ is equal for all configurations with the same neutrino solution. However, when a kinematic fit is applied, the particle momenta are varied and lead to an on average better resolution for $m_{t\bar{t}}$.

8.1.2 Kinematic Fitting

Kinematic fitting in the reconstruction of $t\bar{t}$ events aims at improving the resolution of the measured particle momenta by making use of constraints coming from the $t\bar{t}$ event kinematics

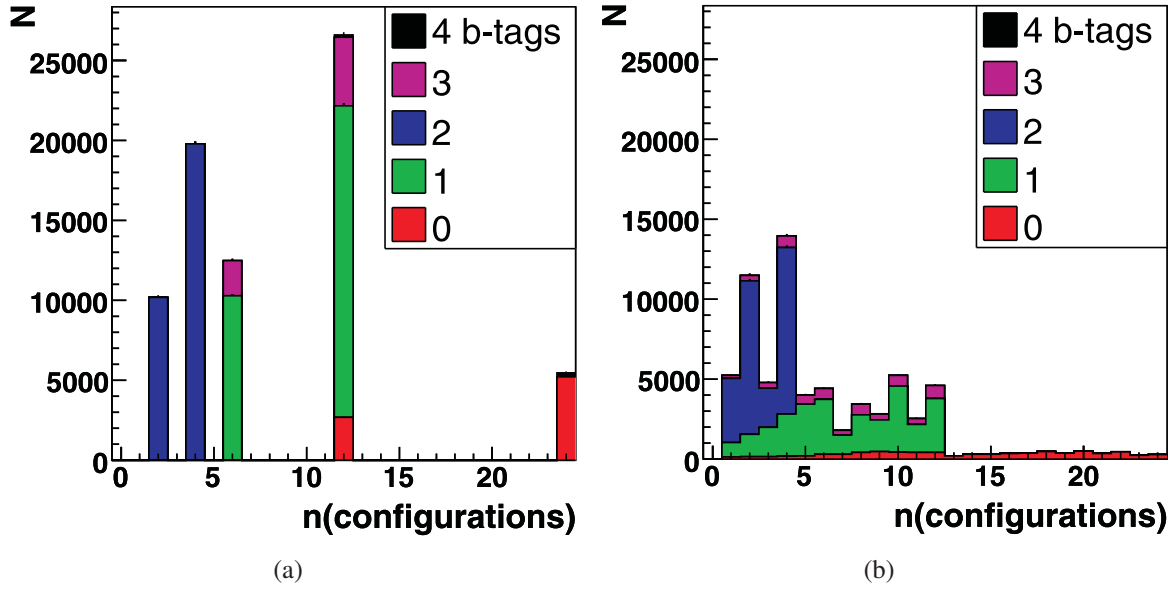(a)   (b)

Figure 8.2: Number of event configurations for semileptonic $t\bar{t}$ events without kinematic fit (a) and with converging kinematic kit (b).

[22,37]. In kinematic fitting, the particle momenta measured in the detector are varied within their uncertainties in order to fulfill these constraints.

The input to a kinematic fit is a list of n measured parameters, $\vec{y}_{input}$ (e.g. the measured particle momenta), their covariance matrix, V, and a list of m constraints , $\vec{f}$ (e.g. mass constraints). The constraints can be linear as well as non-linear functions of the parameters $\vec{y}$ of the form

$$f_i(y_1, y_2, ..., y_n) = 0 \ , \ i = 1...m \ . \tag{8.2}$$

In general the measured parameters $\vec{y}_{input}$ do not fulfill the constraints $\vec{f}$. The task of the kinematic fit is to find parameters $\vec{y}$ that fulfill the constraints $\vec{f}$ and apply a correction $\Delta\vec{y} = \vec{y} - \vec{y}_{input}$ to the measured parameters. The parameters $\vec{y}$ that fulfill the constraints are also required to minimize the χ^2 of the fit given by

$$\chi^2(\vec{y}) = \Delta\vec{y}^T V^{-1} \Delta\vec{y} \ . \tag{8.3}$$

The kinematic fitter implemented in CMSSW uses the method of Lagrange Multipliers to minimize χ^2 and at the same time fulfill the constraints $\vec{f}$. A likelihood defined as

$$L(\vec{y}, \vec{\lambda}) = \chi^2(\vec{y}) + 2\sum_{j=1}^{m} \lambda_j f_j(\vec{y}) \ , \tag{8.4}$$

where $\vec{\lambda}$ are the Lagrange Multipliers is minimized.

The minimization is performed in an iterative procedure to allow the treatment of non-linear constraints. In each iteration step the problem is linearized and solved analytically. The computed parameters $\vec{y}$ are used as input for the next iterative step until certain convergence criteria are fulfilled. These are

$$\chi^2(k-1) - \chi^2(k) < \epsilon_{\chi^2} \ , \tag{8.5}$$

$$F^{(k)} = \sum_{j=1}^{m} f_j^{(k)}(\vec{y}) < \epsilon_F \ . \tag{8.6}$$

where k is the number of iterations. Convergence is therefore achieved when all constraints are fulfilled better than a given value ϵ_F and the improvement in χ^2 from one step to the next step is smaller than a given value ϵ_{χ^2}. In this analysis $\epsilon_{\chi^2} < 0.001$ and $\epsilon_F < 0.001$ are required. If more than 20 iterations are needed to reach convergence, the event configuration is rejected.

For $t\bar{t}$ events three constraints are required to make use of the fact that the $t\bar{t}$ decay chain contains two top quarks and two W bosons which are mostly produced on-shell (with their invariant mass equal to their pole-mass). These constraints are

$$m_{q,\bar{q}} = m_{l,\bar{\nu}} = m_W = 80.403 \text{ GeV} \tag{8.7}$$

$$m_{q,\bar{q},\bar{b}} = m_{l,\bar{\nu},b} . \tag{8.8}$$

where $q,\bar{q}$ correspond to the quarks from the W decay, $l,\bar{\nu}$ to the leptons from the W decay, and $b,\bar{b}$ to the b quarks from the top quark decays as indicated in Figure 8.1. The invariant masses $m_{q,\bar{q}}$, $m_{l,\bar{\nu}}$, $m_{l,\bar{\nu},b}$ and $m_{q,\bar{q},\bar{b}}$ are calculated from the 4-vectors of the corresponding decay products. These are parametrized using three parameters a,b and c in the following way.

$$\vec{p} = a|\vec{p}_m|\vec{u}_1 + b\vec{u}_2 + c\vec{u}_3 \ , \ \vec{u}_1 = \frac{\vec{p}_m}{|\vec{p}_m|} \ , \ \vec{u}_2 = \frac{\vec{u}_3 \times \vec{u}_1}{|\vec{u}_3 \times \vec{u}_1|} \ , \ \vec{u}_3 = \frac{\vec{u}_z \times \vec{u}_1}{|\vec{u}_z \times \vec{u}_1|} \tag{8.9}$$

Here $\vec{p}_m$ corresponds to the measured momenta. The parameters a,b and c give the deviation from $\vec{p}_m$ in three orthogonal directions. This parametrization supports quick convergence of the kinematic fit in contrast to a parametrization in x,y and z directions.

In contrast to the momenta of the decay products, their energy is not varied independently in the kinematic fit but fixed by a mass constraint which gives

$$E = \sqrt{E_m^2 - p_m^2 + p^2} . \tag{8.10}$$

This reduces the number of free parameters in the kinematic fit and leads to a weak constraint on the 4-momenta of the decay products since the masses of the decay products are expected to be small.

The resolutions of the parameters a,b,c have been determined for reconstructed jets, muons, electrons and the missing transverse energy in Ref. [22]. Resolutions are parametrized in bins of η and as a function of E_T using the difference between particle momenta on reconstruction and generator level. The resolutions are filled into the covariance matrix, V, assuming the measured particle momenta to be uncorrelated.

The above described configuration of the kinematic fit leads to a convergence rate of 92.4% for semileptonic $t\bar{t}$ events that pass the pre-selection. The convergence rate corresponds to the fraction of events where the kinematic fit converges for at least one event configuration. The convergence criterion also reduces the number of configurations per event as indicated in Figure 8.2 (b).

In principle the kinematic fit should be able to find the correct neutrino solution unambiguously. If both neutrino solutions given as input to the fit converge to the same neutrino momentum ($\Delta p_z < 2$ GeV), one solution is dropped. However, in the majority of the events the kinematic fit does not converge to the same solution (compare Figure 8.2 (b)). This is due to the fact that the fitter is restricted to finding local minima and not the global minimum.

8.1.3 Choosing Event Configurations

To reach the best resolution in $m_{t\bar{t}}$ one needs to select the correct event configuration. In this analysis the χ^2 from the kinematic fit is used for the selection. In principle it contains information from the overall $t\bar{t}$ event kinematics and should thus be a comprehensive identifier for $t\bar{t}$ events.

To measure the purity of correct event configurations that is achieved by a selection through χ^2, one needs to define a measure that identifies the best event configuration on reconstruction level. For this purpose the reconstructed objects are matched to the objects on generator level. For all combinations of reconstructed jets (leptons) and generated partons (leptons) a distance measure D is calculated,

$$D = \sum_{k=q,\bar{q},\bar{b},b,l} \Delta R(p_{k,\text{reco}}, p_{k,\text{gen}}) \,, \ \ \Delta R(p_i, p_j) = \sqrt{(\phi_i - \phi_j)^2 + (\eta_i - \eta_j)^2} \,. \qquad (8.11)$$

The combination with smallest D is then defined as the best (matched) event configuration.
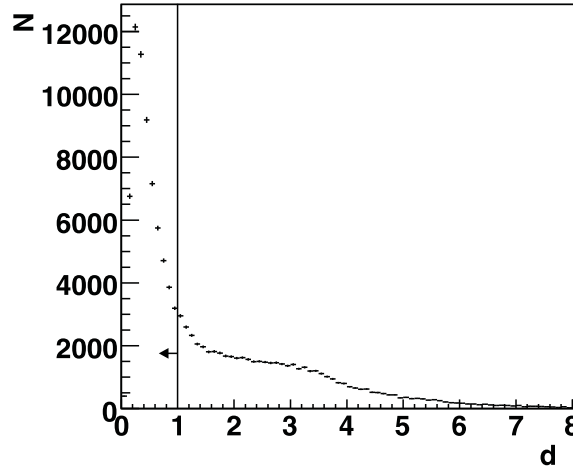
Figure 8.3: Distance measure d for the best event configuration. The vertical line and the arrow indicate the cut defining matched events.

Figure 8.3 shows the distance measure $d = \min(D)$ of the best event configuration. This measure can be used to define which events are reconstructed correctly. As one can see in Figure 8.3 the majority of events has a d smaller than 1. Events with higher d most probably lack reconstructed objects from the $t\bar{t}$ decay. Correctly reconstructed events are thus defined as events with $d < 1$. This choice is of course arbitrary, but motivated by the shape of the distance distribution. With the matching criterion $d < 1$, 53.0% of all pre-selected events with at least four reconstructed jets are identified as correctly reconstructed events.

After event reconstruction using the 4 jets with highest p_T, the fraction of matched event drops to 29.4% . This fraction corresponds to the events with at least one matched event configuration. The reason for this drop are high p_T jets in $t\bar{t}$ events that do not originate from the top quarks themselves, but from initial and final state radiation. These jets are often selected instead of jets from $t\bar{t}$ with lower p_T. The non-matched events thus make up an intrinsic background which needs to be considered in the analysis. Since $m_{t\bar{t}}$ is not reconstructed correctly for these events, they worsen the resolution of $m_{t\bar{t}}$.
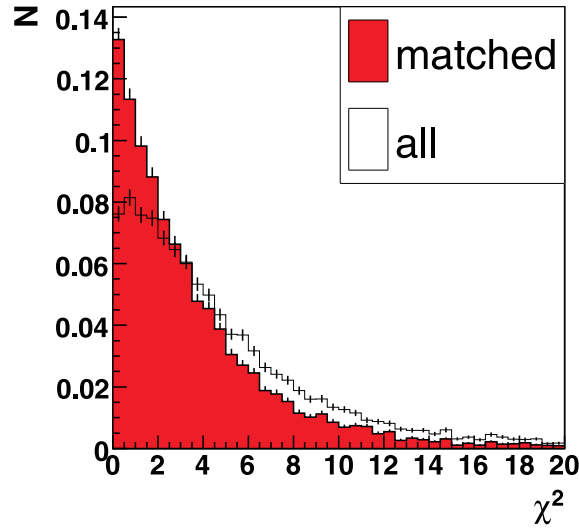
Figure 8.4: χ^2 for matched event configurations (filled histogram) and averaged for all event configurations (open histogram). Both distributions are normalized.

With the matching criterion described above one can measure the separation power of χ^2. Figure 8.4 shows χ^2 for matched event configurations, and averaged for all event configurations. χ^2 exhibits a separation power since matched event configurations accumulate at low χ^2. The fraction of events where the best event configuration is selected by the minimum χ^2 criterion within all matched events is 48% . This number can be compared with the fraction for random selection of event configurations given by the mean over all matched events of $\frac{1}{\text{number of event configurations}} = 29\%$. χ^2 thus proves a good identifier for the best event configuration. In this analysis the event configuration with lowest χ^2 is therefore selected for the reconstruction of $m_{t\bar{t}}$.
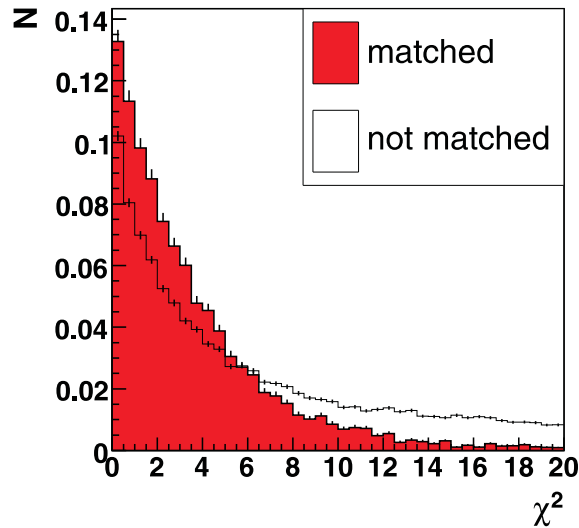
Figure 8.5: Lowest χ^2 for matched events (filled histogram) and non-matched events (open histogram). Both distributions are normalized.

The χ^2 of the selected event configuration can be further used in the analysis. Besides the selection of a best event configuration, χ^2 can also be used as an identifier of correctly reconstructed events. Figure 8.5 shows the χ^2 of matched events and non-matched events. Matched

events clearly accumulate at low χ^2. A cut on χ^2 can thus increase the fraction of correctly identified events and reduce background. This cut will be discussed in the next section.

8.2 The Final Selection

After the kinematic reconstruction of the pre-selected events, a final selection is applied to the events to reduce backgrounds. The final selection aims at reducing two different kinds of background contributions. These are non semileptonic events from other $t\bar{t}$ channels or W+jets production, and intrinsic background from badly reconstructed semileptonic events. Badly reconstructed semileptonic events are events where the wrong event configuration is chosen or where additional objects in the reconstructed events are mistaken as $t\bar{t}$ decay products. The cuts presented here have been optimized for a minimal uncertainty in the top quark mass measurement discussed in detail in Chapter 9.

Figure 8.6 shows all variables used in the final selection. Vertical lines and arrows indicate the cuts applied in the final selection. These are

- ≥ 1 lepton with $p_T > 20$ GeV and $\eta < 2.4$,

- ≥ 4 jets with $p_T > 30$ GeV and $\eta < 2.4$,

- exactly 2 b-tags ,

- $\chi^2 < 4.5$.

The cuts on the number of jets and leptons are necessary for the reconstruction described in Section 8.1. Figure 8.6 (c) and 8.6 (d) show the p_T of the jets with the 4th highest p_T and the p_T of leptons with the highest p_T. The cut on the jet p_T is essential to reduce the W+jets background since W+jets production is typically accompanied by production of jets which have low p_T. The lepton p_T cut is less suited for W+jets background suppression. Therefore it is left at the pre-selection threshold. However, the lepton p_T cut might be a strong handle for the reduction of QCD multi-jet background which is not covered in this analysis.

Another important handle for the reduction of background processes is the requirement of b-tags. In this analysis the impact parameter significance (IPS) of the second track from the track counting algorithm with a cut of $\mathrm{IPS}(2^{\mathrm{nd}}) > 2.3$ is used (see Section 6.2.5). Figure 8.6 (e) shows the number of jets in an event that fulfill this requirement. $t\bar{t}$ events contain two jets from b quarks. Their average number of b-tags is thus around 2. W+jets events as well as QCD multi-jet events on the contrary contain less b quarks. Therefore a cut on the number of b-tags is a strong handle for background reduction.

Figure 8.6 (f) shows the distribution of the χ^2 from the kinematic fit. It does not show a strong separation power for the reduction of the other $t\bar{t}$ and the W+jets backgrounds. However, χ^2 is a good handle for the reduction of intrinsic backgrounds (see Figure 8.5) as already mentioned in Section 8.1.3. By the χ^2 cut, the fraction of matched events is increased from 35.4% to 64.2%. The χ^2 cut is also important for the reduction of systematic uncertainties due to the Jet Energy Scale uncertainties which will be described in Section 9.3.
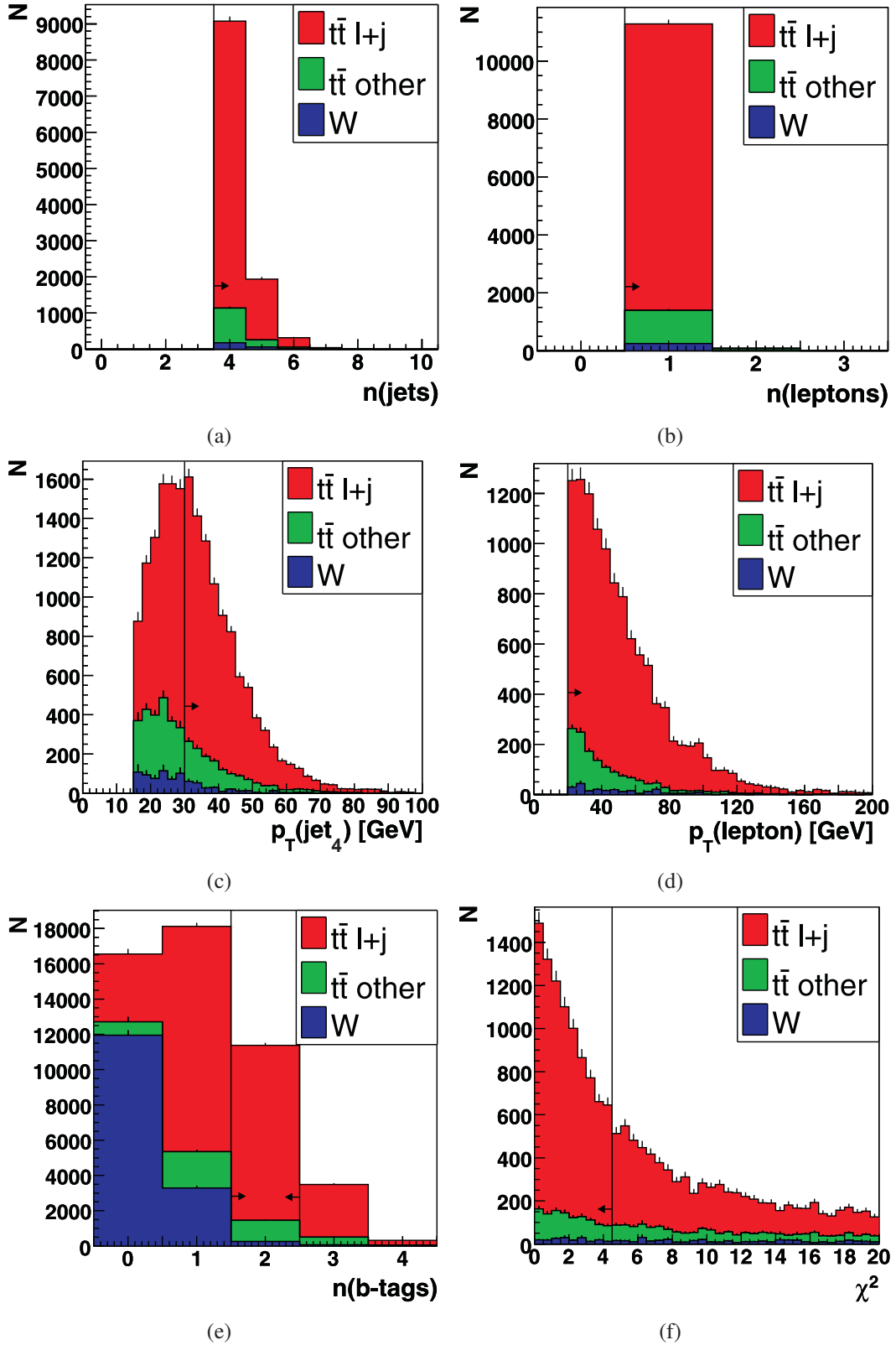
Figure 8.6: Variables used in the final selection. Semileptonic $t\bar{t}$ events, other $t\bar{t}$ events and W+jets events are stacked. Vertical lines and arrows indicate the cuts applied in the final selection. In each plot all cuts of the final selection are applied except for the cut on the variable shown in the plot.
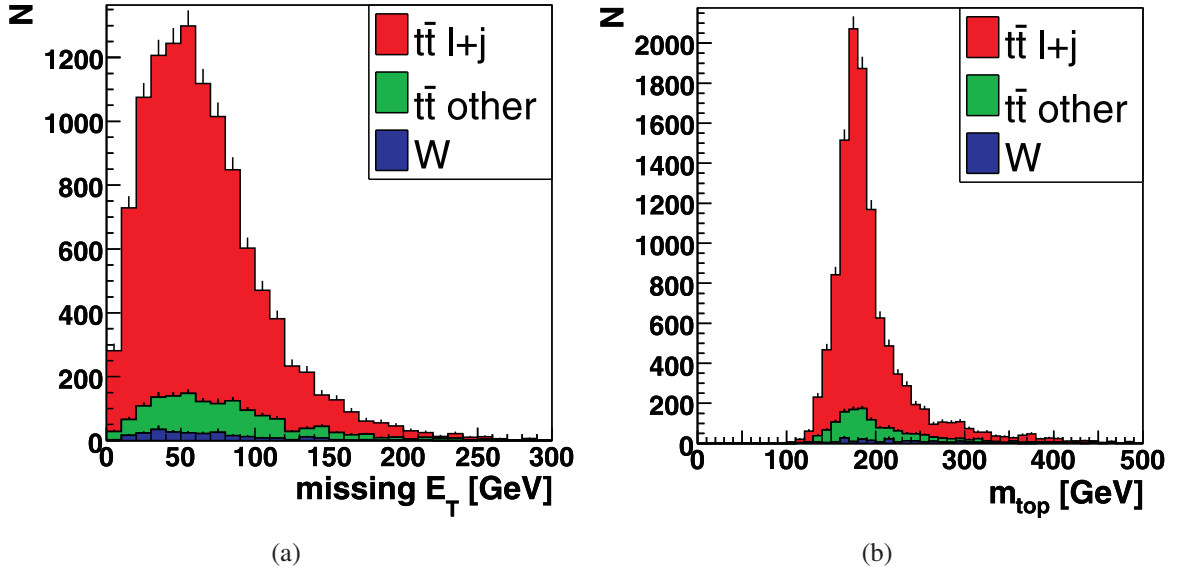
(a)   (b)

Figure 8.7: $\not{E}_T$ and m_{top} after reconstruction and final selection. Semileptonic $t\bar{t}$ events, other $t\bar{t}$ events and W+jets events are stacked.

Figure 8.7 shows the reconstructed $\not{E}_T$ and m_{top} after the final selection. The top quark mass is shown as a control plot since it is not used in the top quark mass measurement in this analysis. The $\not{E}_T$ is shown since it might be an important variable for the reduction of QCD multi-jet background. Typical semileptonic $t\bar{t}$ events have a $\not{E}_T$ of about 50 GeV due to the neutrino in the decay chain. QCD multi-jet events on the contrary do not contain hard neutrinos which produce $\not{E}_T$. Thus $\not{E}_T$ in QCD multi-jet events is mainly due to mis-reconstruction effects.

8.2.1 Selection Efficiencies

The selection efficiencies for semileptonic $t\bar{t}$, other $t\bar{t}$ and W+jets events are summarized in Table 8.1. After all cuts a signal to background ratio of 5:1 is reached, ensuring small impact of the background to the shape to $m_{t\bar{t}}$.

Selection	Number of selected events		
	$t\bar{t}$ semileptonic	$t\bar{t}$ other	W+jets
Total at 1/fb integrated luminosity	248 000	588 000	57 100 000
Pre-selection	143 000	63 900	804 000
Reconstruction (kinematic fit converges)	114 000	40 500	397 000
$p_T(4\,\text{jets}) > 30\,\text{GeV}$	62 900	14 500	37 500
Exactly 2 b-tags	24 800	5 490	1 830
$\chi^2 < 4.5$	8 920	1 510	260

Table 8.1: Number of selected events for semileptonic $t\bar{t}$, other $t\bar{t}$ and W+jets events for $t\bar{t}$ events with $m_{top} = 175$ GeV.
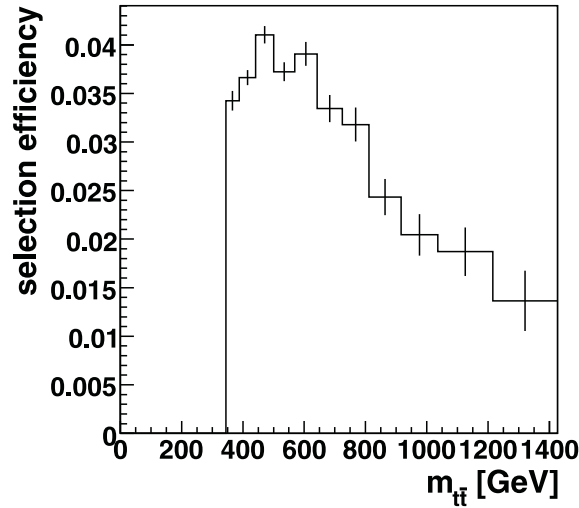
Figure 8.8: Selection efficiency of the final selection for semileptonic $t\bar{t}$ events as a function of $m_{t\bar{t}}$.

Figure 8.8 shows the selection efficiencies of the final selection for semileptonic $t\bar{t}$ events as a function of $m_{t\bar{t}}$. A clear drop in the selection efficiency towards higher $m_{t\bar{t}}$ can be observed. This drop is mainly due to the χ^2 cut which is most effective at high $m_{t\bar{t}}$. At high $m_{t\bar{t}}$ the $t\bar{t}$ decay products have high energies. Since their relative energy resolutions are better at high energies, the χ^2 cut is more sensitive to the $t\bar{t}$ kinematics and is thus able to suppress more badly reconstructed events.

8.2.2 The Precision of the $m_{t\bar{t}}$ Reconstruction

The resolution of $m_{t\bar{t}}$ corresponds to the accuracy that is reached in the reconstruction of $m_{t\bar{t}}$ in one event. It is mainly limited by the resolution of the *Hadronic Calorimeter* which is used for measuring jet energies.

Figure 8.9 shows the difference of reconstructed $m_{t\bar{t}}$ and generated $m_{t\bar{t}}$, $m_{t\bar{t}}^{\text{reco}} - m_{t\bar{t}}^{\text{gen}}$, for three scenarios. In Figure 8.9 (a) no kinematic fit is applied. Three effects can be observed. The reconstructed $m_{t\bar{t}}$ is on average 37.6 GeV higher than the generated $m_{t\bar{t}}$. This is due to the miscalibration of jets and wrongly selected jets. In the central part the distribution can be approximated with a Gaussian function. The Gaussian fit shown in Figure 8.9 (a) gives $\sigma = 67.7$ GeV for the width of the distribution which roughly corresponds to the resolution of $m_{t\bar{t}}$. The third feature of the distribution is a large tail towards high $m_{t\bar{t}}^{\text{reco}} - m_{t\bar{t}}^{\text{gen}}$ due to wrongly reconstructed events.

In Figures 8.9 (b) and (c) the kinematic fit is applied. While in (b) no cut on χ^2 is applied, it is applied in (c). One can observe that all three effects described above improve due to the kinematic fit as well as to the χ^2 cut. The shift towards higher $m_{t\bar{t}}$ is reduced to 11.9 GeV and 10.2 GeV, respectively. The width of the distribution is reduced to 63.3 GeV and 50.7 GeV, respectively. Further, the tail of the distribution is reduced significantly as well.

In this analysis the resolution of $m_{t\bar{t}}$ is defined such that it considers the first and the second effect. Figure 8.10 shows the absolute value of the difference of the reconstructed and generated

(a)

(b)

(c)
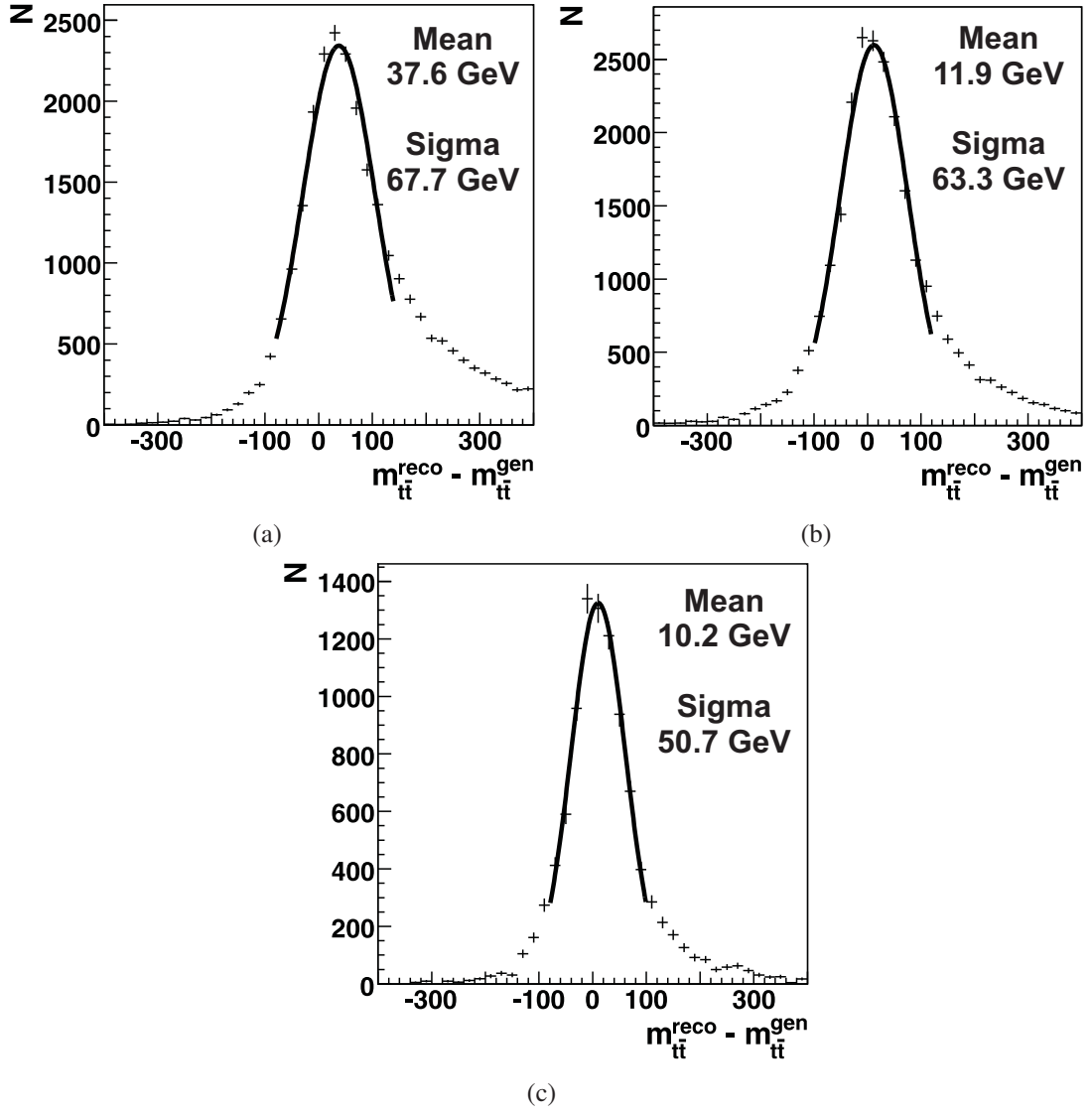
Figure 8.9: The difference of reconstructed and generated $m_{t\bar{t}}$ (a) without kinematic fit, (b) with kinematic fit and without cut on χ^2 and (c) with cut on χ^2.
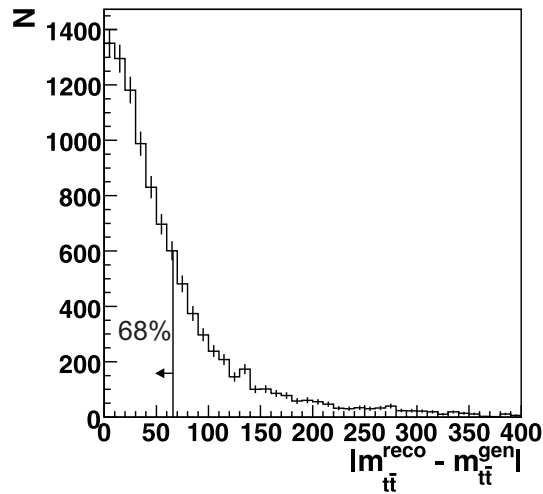

Figure 8.10: Definition of the resolution of $m_{t\bar{t}}$ calculated from $|m_{t\bar{t}}^{\text{reco}} - m_{t\bar{t}}^{\text{gen}}|$.
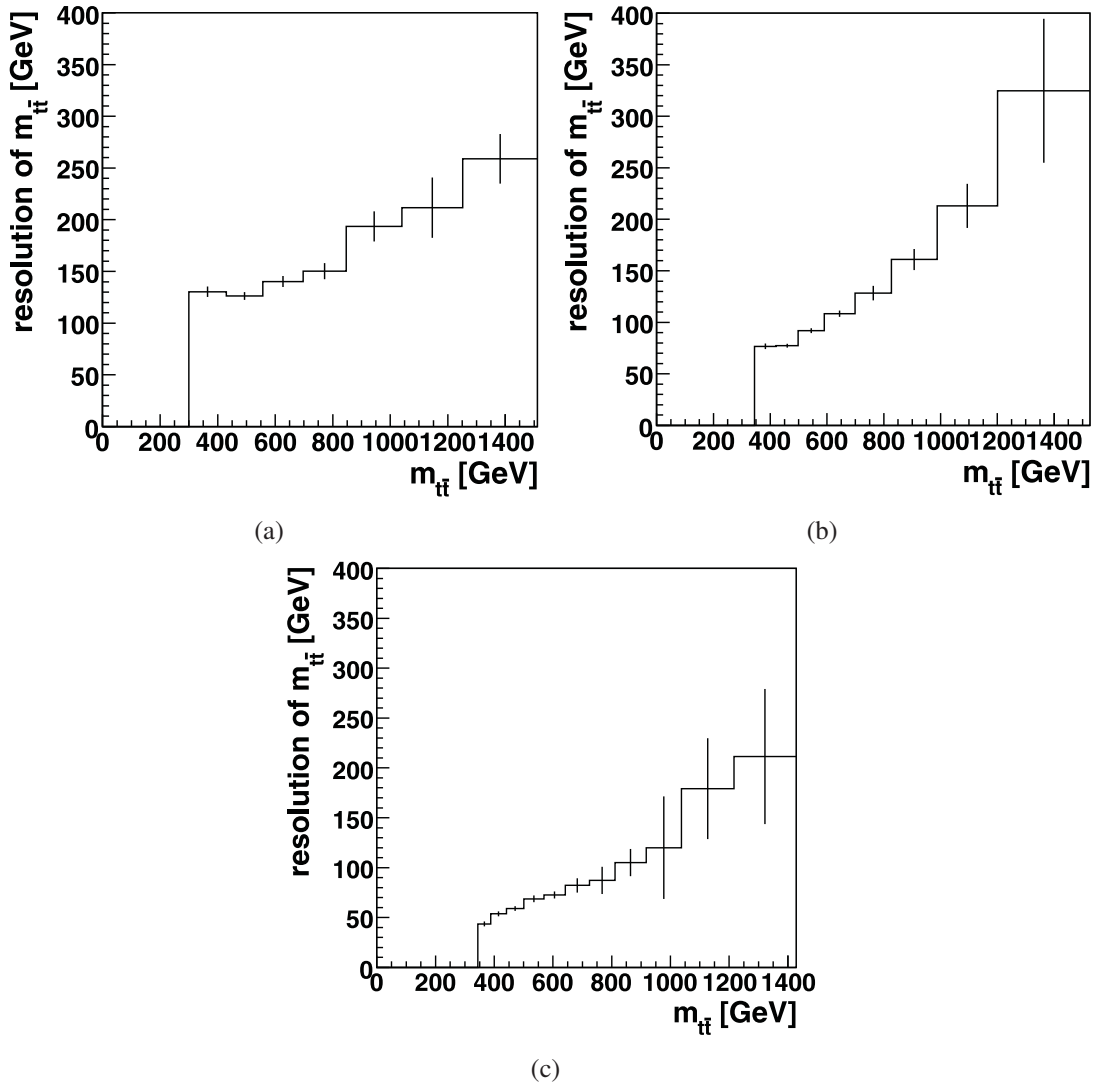
(a)

(b)

(c)

Figure 8.11: Resolution of $m_{t\bar{t}}$ as a function of $m_{t\bar{t}}$ (a) without kinematic fit, (b) with kinematic fit and without cut on χ^2 and (c) with cut on χ^2. Binning according to the resolution of $m_{t\bar{t}}$.

$m_{t\bar{t}}$ ($|m_{t\bar{t}}^{\text{reco}} - m_{t\bar{t}}^{\text{gen}}|$). The resolution of $m_{t\bar{t}}$ is here defined as the value of $|m_{t\bar{t}}^{\text{reco}} - m_{t\bar{t}}^{\text{gen}}|$ that contains 68% of all events with smaller values of this difference.

Figure 8.11 shows the resolution of $m_{t\bar{t}}$ as a function of $m_{t\bar{t}}$ for three scenarios. The kinematic fit as well as the cut on χ^2 improve the resolution. The improvement is mainly observed at low $m_{t\bar{t}}$. This is due to the fact that the relative resolutions of the reconstructed objects are worst at low $m_{t\bar{t}}$. The fit thus achieves highest improvements. At lowest $m_{t\bar{t}}$ resolutions of 130 GeV, 80 GeV and 44 GeV are reached in the three scenarios. At 1 TeV resolutions of 193 GeV, 181 GeV and 120 GeV are still achieved.

8.3 Results for m$_{t\bar{t}}$

Figure 8.12 shows the distribution of the reconstructed $m_{t\bar{t}}$. The binning is done with respect to the resolution of $m_{t\bar{t}}$. Semileptonic $t\bar{t}$, other $t\bar{t}$ and W+jets events are stacked and normalized

to $1/\text{fb}$ of integrated luminosity. The overall shape of the $m_{t\bar{t}}$ distribution on generator level (see Figure 3.5) is reproduced. The threshold at $2m_{top}$ can be observed. The decline at high $m_{t\bar{t}}$ is enhanced in comparison to the generator distribution due to the reduced selection efficiency (see Figure 8.8).
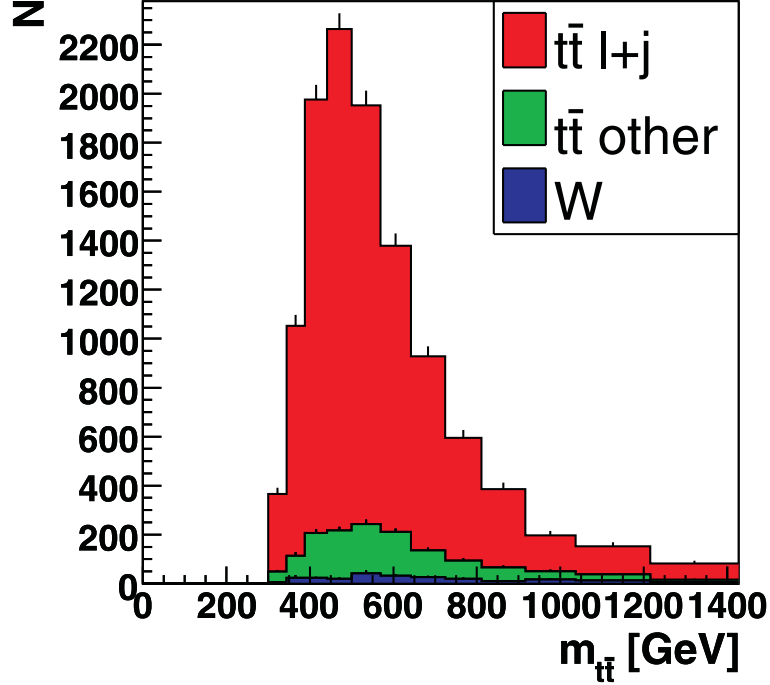
Figure 8.12: Reconstructed $m_{t\bar{t}}$ binned with respect to the resolution. Semileptonic $t\bar{t}$, other $t\bar{t}$ and W+jets events are stacked and normalized to $1/\text{fb}$ of integrated luminosity.

The presented reconstruction of $m_{t\bar{t}}$ achieves a resolution of at best 44 GeV and a signal to background ratio of 5:1. The essential tool to reach this improved resolution is the kinematic fit in combination with a cut on χ^2.

9 Top Quark Mass Measurement from $\mathbf{m}_{t\bar{t}}$

In this chapter a method for a measurement of the top quark mass from $m_{t\bar{t}}$ will be described. The idea of this method is to solely use the $m_{t\bar{t}}$ distribution for a top quark mass measurement in order to avoid systematic uncertainties from the definition of the top quark mass involved in common methods (see Chapter 3).

The top quark mass is extracted from the $m_{t\bar{t}}$ distribution by comparison with template distributions for different top quark masses. In Section 9.1 a detailed description of the template method will be given. Uncertainties on the measured m_{top} will be discussed in Section 9.2. After evaluation of the systematic uncertainties, the cuts involved in the analysis are optimized for a minimal overall uncertainty. This procedure is described in Section 9.3.

9.1 The Template Method

The idea of the template method is to extract the top quark mass by comparing a measured kinematic distribution to template distributions with different top quark masses. The template method is a widespread analysis technique in top quark analyses [6,7]. In common top quark mass analyses the distribution of the invariant mass of the top quark is used in the template method. In this analysis however $m_{t\bar{t}}$ is used instead.

In order to use the shape information of $m_{t\bar{t}}$ and not take into account cross section information, the $m_{t\bar{t}}$ distribution is normalized. This avoids uncertainties involved in cross section measurements, such as the uncertainty on the luminosity measurement which is typically of order 5% [9].

Figure 9.1 shows the reconstructed $m_{t\bar{t}}$ distribution for three different top quark masses which will be called 'templates' in the following. Overall this analysis makes use of 7 templates for the top quark masses of 155 GeV, 165 GeV, 172 GeV, 175 GeV, 178 GeV, 185 GeV and 195 GeV. The templates are combined from $t\bar{t}$ samples and W+jets background. The shape of the different templates can clearly be distinguished using the presented reconstruction strategy. A comparison of the shape of the $m_{t\bar{t}}$ distribution reconstructed from data with the template distributions thus allows a top quark mass measurement.

The comparison of data and templates is done using a binned log-likelihood method. The binned log-likelihood method uses the complete shape information of the distribution and takes into account the statistical uncertainties from the measurement.
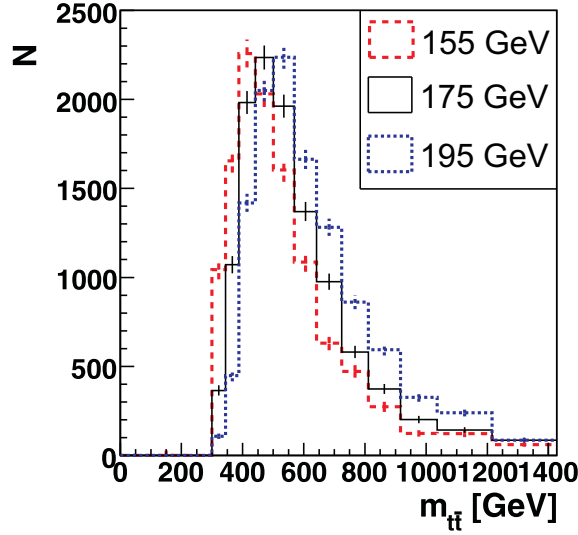
Figure 9.1: Reconstructed $m_{t\bar{t}}$ distribution for three different top quark masses.

The binned log-likelihood method used here is based on Poisson statistics [38]. The likelihood that gives the probability of measuring x events if μ events are expected is given by

$$L(x \mid \mu) = P_\mu(x) = \frac{\mu^x}{x!}e^{-\mu} \, , \tag{9.1}$$

and is normalized by $\int L(x \mid \mu)dx = 1$. The most probable value for μ when measuring x data events is then given by the maximum of the function $L(x \mid \mu)$ with respect to μ. For convenience usually the log-likelihood given by

$$-lnL(x \mid \mu) = -xln\mu + \mu - ln(x!) \tag{9.2}$$

is minimized instead. The likelihood giving the probability of measuring a histogram with the entries x_i in N bins if the entries μ_i are expected is then given by the product

$$L(x_1, ...x_N \mid \mu_1, ..., \mu_N) = \prod_{i=1}^{N} P_{\mu_i}(x_i) \, . \tag{9.3}$$

The binned log-likelihood is therefore defined as

$$-lnL(x_1, ...x_N \mid \mu_1, ..., \mu_N) = \sum_{i=1}^{N} -x_i ln\mu_i + \mu_i - ln(x_i!) \, . \tag{9.4}$$

Since the last term is independent of μ_i it can be dropped for convenience. The binned log-likelihood used here for the m_{top} measurement from $m_{t\bar{t}}$ is

$$-lnL(m_{top}) = \sum_{i=1}^{N} -m_{t\bar{t}}(\text{data})_i \cdot ln(m_{t\bar{t}}(m_{top})_i) + m_{t\bar{t}}(m_{top})_i \tag{9.5}$$

where $m_{t\bar{t}}(\text{data})$ corresponds to the data distribution and $m_{t\bar{t}}(m_{top})$ to the template with top quark mass m_{top}.

In order to test a measurement of m_{top} using the binned log-likelihood method a pseudo-data sample is needed. A sample composed from a $t\bar{t}$ sample with $m_{top} = 175$ GeV and W+jets
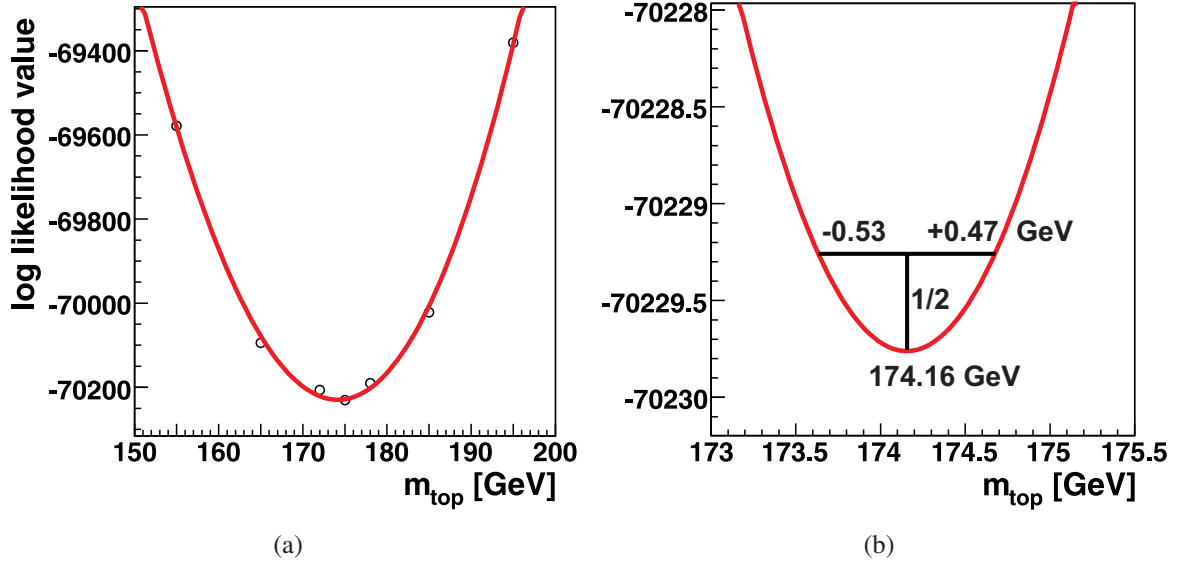
Figure 9.2: Binned log-likelihood value for the 7 top quark mass templates (circles) and a polynomial fit of rank 3 (line). Figure (b) is a scaled view of (a).

background is chosen as pseudo-data. Figure 9.2 shows the resulting binned log-likelihood values as a function of the the top quark masses of the 7 templates.

The shape of the log-likelihood distribution is parabolic which is expected for a log-likelihood close to its minimum. m_{top} can be measured from this distribution by finding the minimum. For this purpose a polynomial of rank 3 is fitted to the likelihood distribution and the minimum of this function is evaluated. The statistical error on m_{top} evaluated in this way is then, by definition of the log-likelihood, given by the width of the distribution at the minimum value plus $1/2$ as indicated in Figure 9.2 (b).

The measured m_{top} of 174.16 GeV does not exactly correspond to the input m_{top} of 175 GeV. Also, a closer look at the log-likelihood distribution shows deviations from the parabolic shape. These are due to the fact that each bin content of the $m_{t\bar{t}}$ distribution does not depend linearly on m_{top} in the examined m_{top} range. Additionally there is an influence due to limited Monte Carlo statistics which needs to be taken into account in the evaluation of the uncertainties. In Section 9.2.3 a potential bias due the fitting of the not perfectly parabolic distribution will be discussed.

9.2 Uncertainties

9.2.1 The Statistical Uncertainty

The statistical uncertainty derived from Figure 9.2 (b) which corresponds to an integrated luminosity of $1/\text{fb}$ is

$$\sigma_{\text{stat}}(1/\text{fb}) = {}^{+0.47}_{-0.53}\,\text{GeV}\,. \tag{9.6}$$

The evaluation of the statistical uncertainty from the log-likelihood distribution relies on a perfect description of the template samples. Since the Monte Carlo statistics of the templates is limited the evaluated statistical uncertainty needs to be validated. Therefore, pseudo experiments are carried out. Using the data distribution as input, 1000 pseudo-data distributions are diced according to a Poisson distribution for each bin of the $m_{t\bar{t}}$ distribution. For each set of pseudo-data, the top quark mass is measured using the log-likelihood distribution. The resulting top quark masses are then filled in a histogram, shown in Figure 9.3.
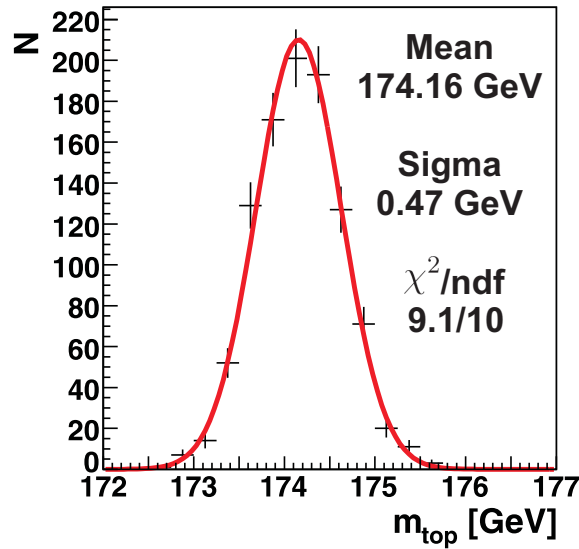
Figure 9.3: The measured top quark mass evaluated from pseudo experiments.

The distribution of the top quark masses from pseudo experiments is in perfect agreement with a Gaussian distribution. A fit of a Gaussian function yields a $\chi^2/\mathrm{ndf} = 9.1/10$. The Gaussian is centered at 174.16 GeV which is equal to the top quark mass determined for the data distribution. This confirms that the top quark mass determination from the log-likelihood distribution is stable. The width of the Gaussian corresponds to the statistical uncertainty. By construction it should be equal to the statistical error from the log-likelihood distribution. The estimated width of 0.47 GeV confirms this fact.

Figure 9.4 shows the expected statistical uncertainty of m_{top} as a function of the integrated luminosity. The statistical uncertainty of m_{top} behaves like the statistical error of a mean, proportional to $\frac{1}{\sqrt{N}}$, where N is the number of events which is directly proportional to the integrated luminosity. A fit yields

$$\sigma_{stat} = \frac{0.53 \text{ GeV}}{\sqrt{L/\mathrm{fb}^{-1}}} \tag{9.7}$$

According to this formula a statistical uncertainty of 1 GeV can be reached with an integrated luminosity of $0.28/\mathrm{fb}$.

One should note that the $t\bar{t}$ cross section, calculated for a top quark mass of 175 GeV, enters in this formula. For a top quark mass of 170 GeV the $t\bar{t}$ cross section is 15% higher, resulting in a 7 % smaller statistical uncertainty at $1/\mathrm{fb}$ integrated luminosity. Further, trigger efficiencies have not been taken into account in this analysis. Assuming an average trigger efficiency of 80% (see Section 7.2.1) the statistical uncertainty becomes 12 % higher at $1/\mathrm{fb}$ integrated luminosity.
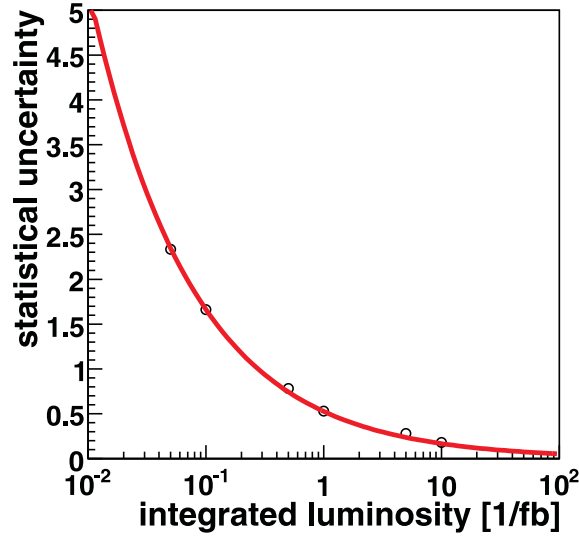
Figure 9.4: Expected statistical uncertainty of m_{top} as of function of the integrated luminosity.

9.2.2 The Jet Energy Scale Uncertainty

The uncertainty on the calibration of the Jet Energy Scale (JES) is the main systematic uncertainty in the measurement of the top quark mass determined from $m_{t\bar{t}}$. For 1-10/fb of integrated luminosity, the calibration from the hadronic W boson mass in $t\bar{t}$ events [39] is expected to be the most accurate method for a determination of the absolute JES [40]. An accuracy of 3% is expected for this method. Due to a jet p_T cut of 30 GeV in the W boson calibration, the method is limited to high p_T jets. Low p_T jets need to be calibrated using the γ+jets method with an uncertainty of order 10% [41]. It is therefore recommended to expect higher systematic uncertainties of up to 10% below a jet p_T of 50 GeV.

In this analysis the systematic uncertainty on the absolute JES of 3% is taken into account, while uncertainties due the non-linearity are postponed to analyses based on a calibration with real data. In principle a non-linearity of the JES may have a sizable impact on the shape of the $m_{t\bar{t}}$ distribution and needs to be considered additionally to the uncertainty on the absolute JES.

The impact of the JES uncertainty on the measured m_{top} is calculated by applying shifts on the JES of the data sample and measuring the resulting shift of the measured m_{top}. Figure 9.5 shows the shift of the measured m_{top} as a function of the JES shift[1]. A linear dependence is observed which can be approximated by a linear fit. For a reconstruction without kinematic fit (see Figure 9.5 (a)) the fit yields a slope of

$$\frac{\Delta m_{top}}{\Delta \text{JES}} = 1.56 \frac{\text{GeV}}{\%} \ . \tag{9.8}$$

For the full reconstruction with kinematic fit and cut on χ^2 (see Figure 9.5 (b)), the fit yields a slope of

$$\frac{\Delta m_{top}}{\Delta \text{JES}} = 0.85 \frac{\text{GeV}}{\%} \ . \tag{9.9}$$

---

[1]Note that Figure 9.5 does not show error bars. The statistical fluctuations of the measured m_{top} shifts are due to the limited Monte Carlo statistics of the data sample of $\Delta m_{top} = ^{+0.47}_{-0.53}$ GeV. However, since the same Monte Carlo sample with shifted JES was used for all points, the samples are highly correlated and the observed fluctuations are smaller than those expected from the Monte Carlo statistics.
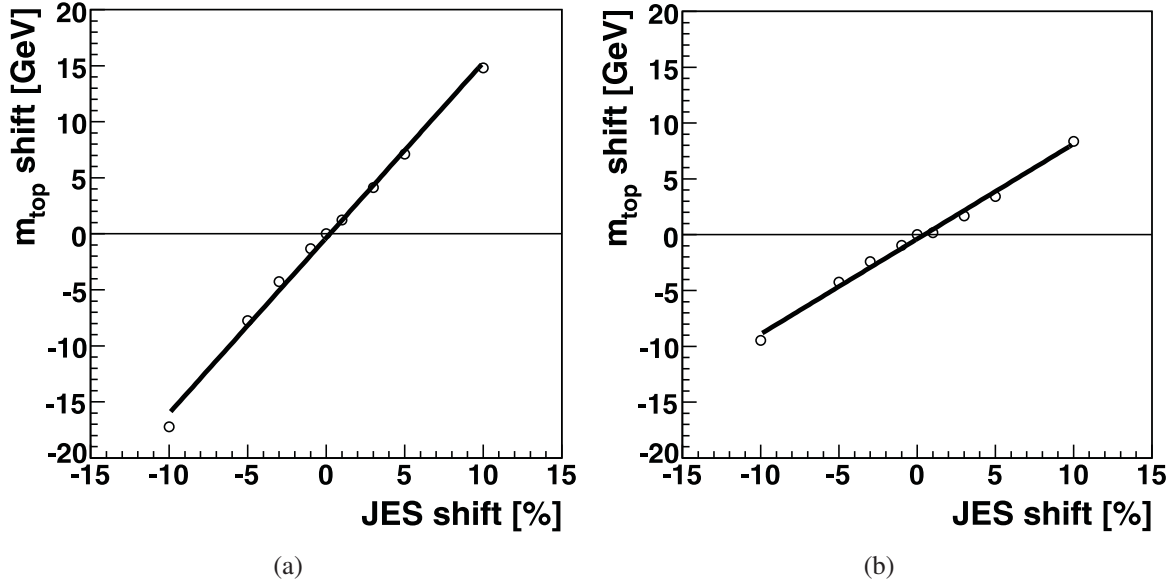
Figure 9.5: Top quark mass shift as a function of the JES shift (a) without kinematic fit and (b) with kinematic fit and cut on χ^2.

The dependence of the JES uncertainty on the measured m_{top} is thus reduced by the kinematic fit with the cut on χ^2. This is due to the fact that the χ^2 cut is equivalent to a cut on the deviation from the W mass constraint. Events with wrongly calibrated jets are thus cut away.

The JES uncertainty of 3% at 1/fb for the full reconstruction with kinematic fit and cut on χ^2 leads to an uncertainty on the measured m_{top} of

$$\sigma_{\text{JES}}(1/\text{fb}) = \begin{smallmatrix} +1.68 \\ -2.41 \end{smallmatrix} \text{GeV} . \tag{9.10}$$

A JES shift has direct impact on the $\not{E}_T$ through the corresponding correction

$$\vec{\not{E}}_T^{corr} = \vec{\not{E}}_T - \sum_i \vec{p}_i^{\,corr} - \vec{p}_i^{\,raw} . \tag{9.11}$$

This shift has been taken into account for jets with $p_T > 20$ GeV in the evaluation of σ_{JES}. However, the $\not{E}_T$ has significant contributions from low p_T jets and unclustered energy which will not be understood to better than 10% at 1-10/fb of integrated luminosity [40]. The low p_T component of $\vec{\not{E}}_T$, which is equal to $\vec{\not{E}}_T^{corr} - \sum_i p_i^{\,corr}$, is therefore varied by 10% uncorrelated from the high p_T component of $\vec{\not{E}}_T$, resulting in an uncertainty on m_{top} of

$$\sigma_{\text{low } \not{E}_T}(1/\text{fb}) = \begin{smallmatrix} +0.45 \\ -0.73 \end{smallmatrix} \text{GeV} . \tag{9.12}$$

9.2.3 Systematic Uncertainties resulting from the Likelihood Method

The method of measuring m_{top} from the log-likelihood distribution may have an intrinsic bias. Possible sources are the limited Monte Carlo statistics of the templates and the polynomial fit of
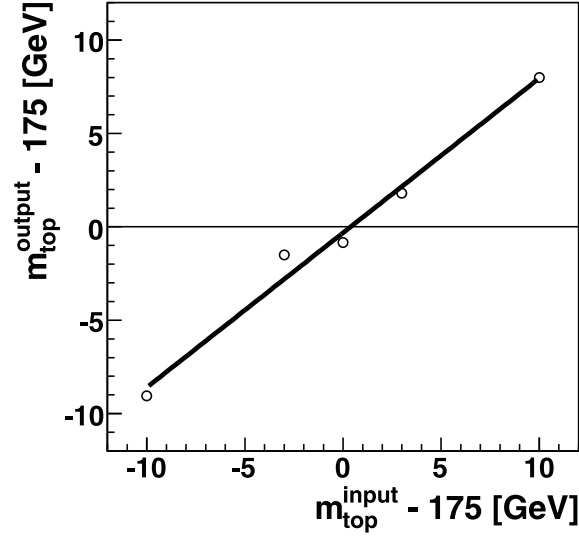
Figure 9.6: Measured $m_{top}-175$ GeV as a function of the $m_{top}-175$ GeV of the input data.

the log-likelihood distribution. To investigate a possible bias, the method is tested with different data distributions with different m_{top}.

Figure 9.6 shows the measured $m_{top}-175$ GeV as a function of the $m_{top}-175$ GeV of the input data. A linear dependency is observed. The slope determined by a linear fit is

$$\frac{m_{top}^{\text{measured}} - 175 \text{ GeV}}{m_{top}^{\text{input}} - 175 \text{ GeV}} = 0.827. \tag{9.13}$$

For a perfect measurement method for m_{top} a slope equal to 1 is expected. Mostly due to the non-perfect polynomial fit, the slope is reduced. Besides the reduced slope, also a shift of

$$m_{top}^{\text{measured}} - 175 \text{ GeV} = -0.32 \text{ GeV} . \tag{9.14}$$

is observed. Both slope and shift can be easily corrected for by the following function,

$$m_{top}^{\text{corr}} = 175 \text{ GeV} + \frac{1}{0.827}(m_{top}^{\text{measured}} - 175 \text{ GeV} + 0.32 \text{ GeV}) . \tag{9.15}$$

Figure 9.7 shows the difference between the corrected m_{top} and the input m_{top} for five different data samples with different m_{top}. One can observe that the corrected m_{top} scatterers around the input m_{top}. This is mostly due to the limited Monte Carlo statistics of the templates. Since the Monte Carlo statistics of the templates corresponds to about $500/\text{pb}$, statistical fluctuations of order 0.75 GeV are expected from Equation (9.7). The Root Mean Square (RMS) of the five m_{top} shifts in Figure 9.7 of

$$\sigma_{\text{bias}} = 0.82 \text{ GeV} \tag{9.16}$$

is in well agreement with these expected fluctuations. Both, the uncertainty from the limited Monte Carlo statistics as well as a possible bias from the polynomial fit, can in principle be completely eliminated by sufficient Monte Carlo statistics and a sufficient high number of template samples. It is thus not included in the expected overall uncertainty.
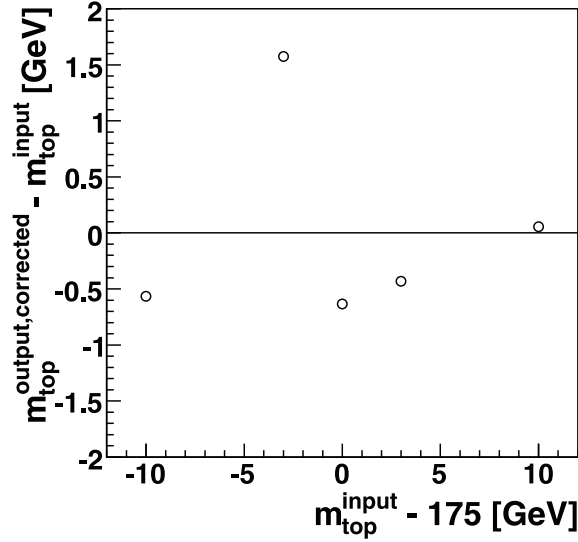
Figure 9.7: The difference between the corrected m_{top} and the input m_{top} as a function of the input m_{top}.

9.2.4 Other Systematic Uncertainties

The uncertainty of the b-tag efficiency and the mistag rate assumed in the Monte Carlo samples are another source of systematic uncertainty on the top quark mass measurement from $m_{t\bar{t}}$. For a minimal dependence on the detector simulation, they need to be determined from data. The expected uncertainty on the b-tag efficiency is about 6% in the barrel region and about 10% in the endcaps [28]. The uncertainty of the mistag rate is assumed to be 5% [9].

To evaluate the resulting uncertainty on the measured m_{top} from the uncertainty of the b-tag efficiency, 6% (10%) of all b-tagged jets with $|\eta| < 1.5$ ($|\eta| \geq 1.5$) are untagged randomly. The evaluated uncertainty on m_{top} is

$$\sigma_{\text{tag eff}}(1/\text{fb}) = 0.09 \text{ GeV} . \tag{9.17}$$

The uncertainty from the mistag rate uncertainty is obtained by randomly (mis-)tagging non-tagged jets. Since 10% of all jets are mis-tagged in average, additional 5% × 10% of the non tagged jets are (mis-)tagged to evaluate the resulting uncertainty on m_{top} which is

$$\sigma_{\text{mis tag}}(1/\text{fb}) = 0.11 \text{ GeV} . \tag{9.18}$$

Another source of systematic uncertainties are the uncertainties of the cross sections assumed in the Monte Carlo samples. The impact of these uncertainties on the m_{top} measurement is expected to be small since the $m_{t\bar{t}}$ distribution is normalized in the analysis. The ratio of different processes does however have an impact on the shape of $m_{t\bar{t}}$.

Theoretical calculations predict a cross section of 833 pb for the $t\bar{t}$ production with an uncertainty of ±5% from the variation of the scales $\mu_F = \mu_R$ and ±3% from uncertainties of the parton distribution functions (PDFs) [42]. In principle the scales μ_F and μ_R need to be varied

independently resulting in a larger uncertainty [10]. In this analysis an overall uncertainty of $\pm 6\%$ will be assumed, resulting in an uncertainty on m_{top} of

$$\sigma_{t\bar{t}} = {}^{+0.021}_{-0.024} \text{ GeV} . \tag{9.19}$$

A recent prediction for the W+jets cross section is 9370 ± 870 pb [43]. This gives an uncertainty on m_{top} of

$$\sigma_{W+\text{jets}} = {}^{+0.033}_{-0.034} \text{ GeV} . \tag{9.20}$$

Another possible source of systematic uncertainties is the use of the *Fast Simulation* for the generation of the template samples, since the *Fast Simulation* uses a less detailed description of the detector response than the *Full Simulation*. In principle the impact of the *Fast Simulation* on the $t\bar{t}$ kinematics needs to be studied in detail. In this analysis a detailed comparison was, however, impossible due to the use of different software versions for the *Fast Simulation* and *Full Simulation* samples. The use of a semileptonic $t\bar{t}$ sample generated with *Full Simulation* instead of the *Fast Simulation* semileptonic $t\bar{t}$ sample as data sample leads to shift in m_{top} of

$$\sigma_{\text{fastsim}} = 0.42 \text{ GeV} . \tag{9.21}$$

Due to the different software versions used for reconstruction, this value needs to be regarded as an upper limit for the systematic uncertainty from the use of the *Fast Simulation*. This systematic uncertainty can in principle be avoided by using the *Full Simulation* for all template samples and is thus not included in the expected overall uncertainty.

One should note that there are several other sources of systematic uncertainties in the modeling of the Monte Carlo samples which are not covered in this analysis. These are the PDFs entering the Monte Carlo, the modeling of showering and hadronization, the description of the underlying event as well as Pile-Up.

Taking into account all examined uncertainties, the overall uncertainty on the measured top quark mass at $1/\text{fb}$ is given by

$$\sigma = \sigma_{\text{stat}} \oplus \sigma_{\text{JES}} \oplus \sigma_{\text{low } \not{E}_T} \oplus \sigma_{\text{tag eff}} \oplus \sigma_{\text{mis tag}} \oplus \sigma_{t\bar{t}} \oplus \sigma_{W+\text{jets}} = 2.57 \text{ GeV} . \tag{9.22}$$

All uncertainties are assumed to be uncorrelated and thus added quadratically.

9.3 Cut Optimization for the Final Selection

The goal of this analysis is to estimate the expected uncertainties on a top quark mass measurements from $m_{t\bar{t}}$. Therefore, the analysis should be optimized for a minimal overall uncertainty. In common top quark mass analyses at the Tevatron the statistical uncertainty is usually minimized, since it is still the dominant uncertainty. In general it is however desirable to minimize the overall uncertainty. The strategy of this analysis is to optimize the cuts involved in the final
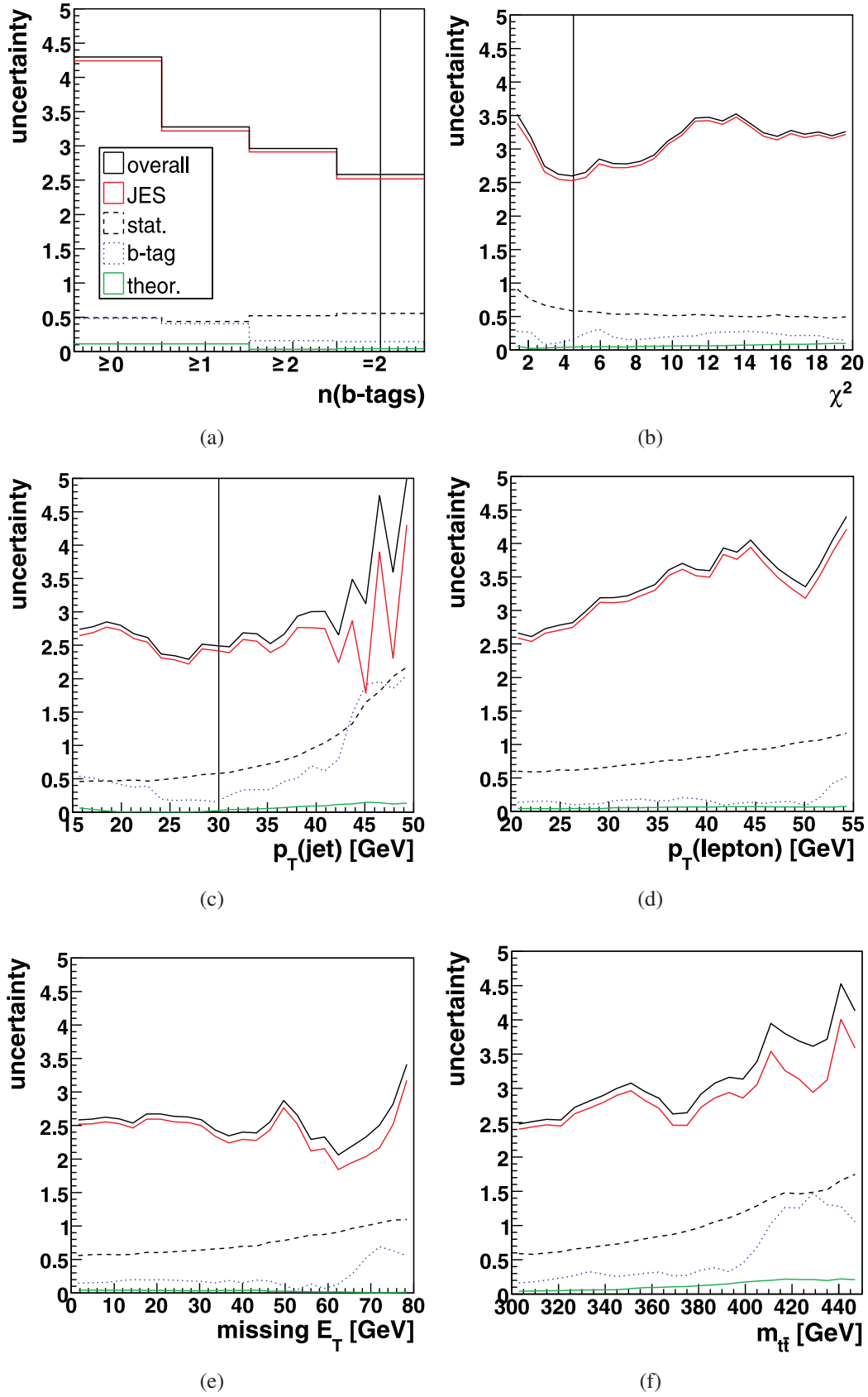
Figure 9.8: Expected uncertainties on the measured m_{top} as a function of several cuts. Vertical lines correspond to the cuts applied in the final selection.

selection for a minimal overall uncertainty. For this purpose the systematic uncertainty has to be calculated for each possible set of cuts.

Figure 9.8 shows the expected uncertainties as a function of several cuts. The uncertainties are defined as

$$\text{JES} = \max(\pm\sigma_{\text{JES}}) \oplus \max(\pm\sigma_{\text{low } \not{E}_T}) \,, \tag{9.23}$$

$$b\text{-tag} = \sigma_{\text{tag eff}} \oplus \sigma_{\text{mis tag}} \,, \tag{9.24}$$

$$\text{stat.} = \max(\pm\sigma_{\text{stat}}) \,, \tag{9.25}$$

$$\text{theor.} = \max(\pm\sigma_{t\bar{t}}) \oplus \max(\pm\sigma_{W+\text{jets}}) \,, \tag{9.26}$$

$$\text{overall} = \text{JES} \oplus b\text{-tag} \oplus \text{stat.} \oplus \text{theor.} \,, \tag{9.27}$$

where $\max(\pm\sigma)$ is the maximum of the of the evaluated upper and lower limits of an uncertainty σ. All uncertainties are calculated for 1/fb of integrated luminosity. The cuts of the final selection are thus optimized for this amount of data. For other luminosities the cuts need to be adjusted.

The optimization is performed in the following way. In principle all cuts of the final selection need to be optimized simultaneously in a multidimensional space. In order to have reasonable computation time several cuts are assumed to be independent and are hence optimized successively. First, reasonable starting values for all cuts are chosen. Then, the number of jets and leptons, the number of b-tags and the χ^2 cut are optimized simultaneously. Afterwards the jet and lepton p_T cuts are regarded. The optimization is iterated twice in order to check for a dependency on the starting values. In principle, the resolution of $m_{t\bar{t}}$ needs to be recalculated for each combination of cuts. In order to limit the computation time, the resolution has only be adjusted when the cuts on the number of jets, leptons and b-tags are changed.

For the number of jets and leptons two different cuts each were investigated.

- number of leptons ≥ 1 or $= 1$

- number of jets ≥ 4 or $= 4$

It was found that both cut combinations lead to differences in the overall uncertainty smaller than 0.2 GeV. Therefore, the cuts with higher acceptance (≥ 4 jets and ≥ 1 lepton) are chosen.

The cut on the number of b-tags (see Figure 9.8 (a)) is essential for the reduction of the overall uncertainty. It turns out that the requirement of exactly 2 b-tags leads to the smallest uncertainty. This cut limits the number of event configurations to a maximum of 4 and also strongly suppresses the W+jets background. As a consequence the uncertainty from the JES calibration is strongly reduced.

The cut on maximum χ^2 from the kinematic fit used in the reconstruction of $m_{t\bar{t}}$ is varied in Figure 9.8 (b). A minimum in the overall uncertainty can be observed around a cut of $\chi^2 < 4.5$. As discussed in Section 9.2.2, the χ^2 cut reduces the uncertainty from the JES calibration. Also, it reduces intrinsic background as discussed in Section 8.2. A too hard cut on χ^2 however increases the statistical uncertainty. Here, a cut of $\chi^2 < 4.5$ is therefore chosen in the final selection.

The cut on the minimum jet p_T (see Figure 9.8 (c)) has almost no impact on the overall uncertainty up to 40 GeV. Higher cut values lead to a drastic increase in the overall uncertainty. An intermediate cut of $p_T > 30$ GeV is therefore chosen. This cut provides well defined and reasonably well calibrated jets. Since the jet p_T cut might also be important for the suppression of the QCD multi-jet background, it is important to note that a variation of this cut does not lead to a significant change of the overall uncertainty.

The cut on the minimum lepton p_T (see Figure 9.8 (d)) is, in contrast to the jet p_T cut, correlated with the overall uncertainty. With increasing lepton p_T the overall uncertainty rises up to a cut at about 45 GeV and runs into a local minimum at 50 GeV. The global minimum is however at lowest p_T. In the final selection a lepton is therefore required to have $p_T > 20$ GeV.

In Figure 9.8 (e) a cut on the minimal $\not{E}_T$ is applied. This cut is mostly uncorrelated with the overall uncertainty. In the final selection no cut is thus applied on $\not{E}_T$. Since a $\not{E}_T$ cut might be an important handle for suppressing the QCD multi-jet background, it is again important to note that this cut has small impact on the overall estimated uncertainty.

Figure 9.8 (f) shows a cut on the minimal reconstructed $m_{t\bar{t}}$. In the region from 300 GeV to 320 GeV, the cut has an impact of less than 0.1 GeV on the overall uncertainty. This is important to note since it shows that the analysis depends very weakly on the choice of the position of the first bin of the $m_{t\bar{t}}$ distribution. Over the whole region from 320 GeV to 450 GeV the overall uncertainty increases with rising cut limit. This is due to the fact that most of the top quark mass information in the shape of the $m_{t\bar{t}}$ distribution is observable in the position of the threshold at $2m_{top}$. If this threshold is cut away, the statistical uncertainty is drastically increased.

9.4 Results for m$_{top}$

Table 9.1 summarize the expected uncertainties of a top quark mass measurement from $m_{t\bar{t}}$ with $1/$fb of integrated luminosity. An overall uncertainty of 2.57 GeV can be reached. With $1/$fb of integrated luminosity at the CMS experiment, this method cannot compete with the accuracy reached by the Tevatron experiments of 1.8 GeV. However, it will be a good cross check, since the presented method does not directly use the invariant mass distribution of the reconstructed top quark, in contrast to the common methods.

An extrapolation to a luminosity of order $10/$fb of the expected uncertainties is shown in Table 9.2. The statistical uncertainty is scaled to $10/$fb using Equation (9.7). For the JES uncertainty an optimistic estimate of 1% is used. Other systematic uncertainties are not regarded. If a JES calibration with an accuracy of 1% was reached at the CMS experiment, a top quark mass measurement with an accuracy of better than 1 GeV could be achieved. Then the systematic uncertainties due to the theoretical definition of the top quark mass and the modeling in the Monte Carlo generators become important. The measurement of m_{top} from $m_{t\bar{t}}$ is then expected to involve different systematic uncertainties than measurements that use the invariant mass of the top quark.

The theoretical systematic uncertainties involved in the top quark mass definition as well as the systematic uncertainties involved in the Monte Carlo modeling, such as the PDFs entering

Uncertainty source	Uncertainty [GeV]	
Statistical error	-0.53	+0.47
JES	-2.41	+1.68
Low $\not{E}_T$	-0.72	+0.45
b-tag efficiency	0.09	
Mistag rate	0.11	
$t\bar{t}$ cross section	-0.024	+0.021
W+jets cross section	-0.034	+0.033
overall	2.57	

Table 9.1: Expected uncertainties on the measured m_{top} for 1/fb of integrated luminosity.

Uncertainty source	Uncertainty [GeV]
Statistical error	0.17
JES	0.85
overall	0.87

Table 9.2: Expected uncertainties on the measured m_{top} for 10/fb of integrated luminosity.

the Monte Carlo, the modeling of showering and hadronization, the underlying event as well as Pile-Up, are not covered in this analysis. A detailed analysis of these effect thus needs to be carried out to clarify if a top quark mass measurement from $m_{t\bar{t}}$ does in fact lead to a lower systematic uncertainty compared to common methods.

From the theoretical point of view a top quark mass measurement from an event shape variable which can be easily compared to a theoretical prediction is desirable. For this purpose, additionally to the above described reconstructed $m_{t\bar{t}}$, two different variables are regarded.

The first variable is the reconstructed $m_{t\bar{t}}$ without use of the kinematic fit. This variable does not use any information on the top quark kinematics except for the fact that the neutrino and the lepton originate from a W boson. The longitudinal component of the neutrino momentum is calculated from the W mass constraint and the solution with smaller p_z is selected.

The second variable is the transverse $m_{t\bar{t}}$ defined by

$$\text{transverse } m_{t\bar{t}} = \sqrt{(E_{t,T} + E_{\bar{t},T})^2 - (\vec{p}_{t,T} + \vec{p}_{\bar{t},T})^2} \, , \tag{9.28}$$

where $\vec{p}_{t,T}$ and $\vec{p}_{\bar{t},T}$ correspond to the two-dimensional momentum vectors in the x-y-plane of the top and the anti-top quark. The transverse $m_{t\bar{t}}$ can be fully measured in the CMS experiment since no information on the longitudinal momentum of the neutrino is needed. It is thus an event shape variable that can be reconstructed by adding the transverse momenta of the four leading jets, the leading lepton and the $\vec{\not{E}}_T$ in an event.

Figure 9.9 shows template distributions for both variables for three different top quark masses. The binning is chosen according to the resolution. The resolution of both variables is much worse in comparison with the standard reconstruction of $m_{t\bar{t}}$ since no kinematic fit is used. Due to its definition the transverse $m_{t\bar{t}}$ is always smaller than $m_{t\bar{t}}$.

(a)   (b)
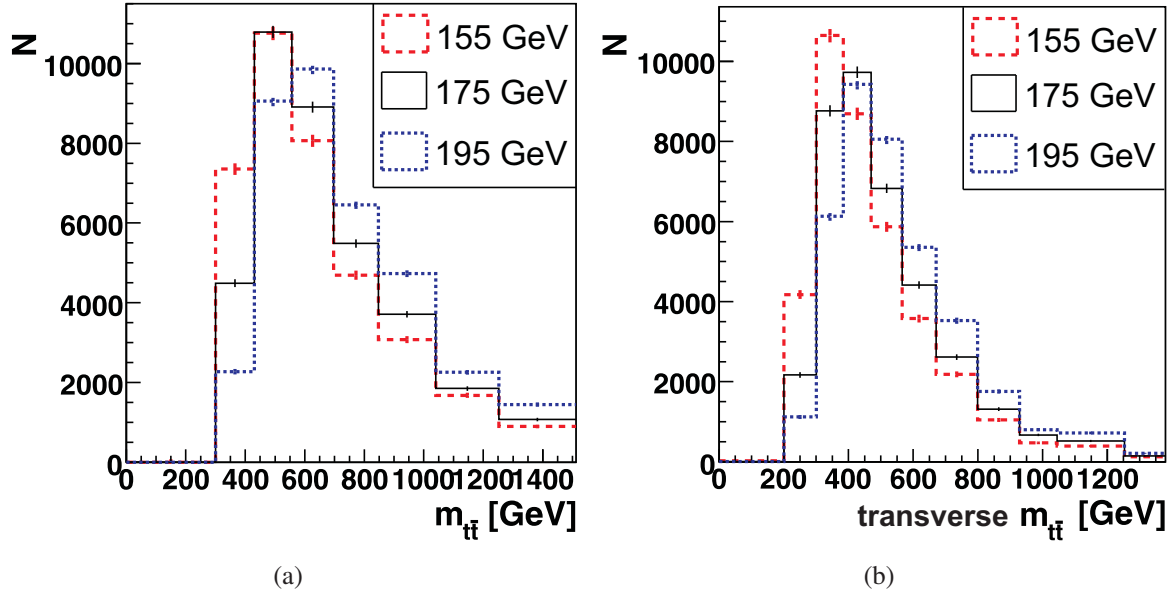
Figure 9.9: Template distributions for three different top quark masses using a reconstruction without the kinematic fit. $m_{t\bar{t}}$ (a) as well as the transverse $m_{t\bar{t}}$ (b) are shown. Binning according to the resolution.

Uncertainty source	Uncertainty [GeV] $m_{t\bar{t}}$		Uncertainty [GeV] Transverse $m_{t\bar{t}}$	
Statistical error	-0.45	+0.40	-0.42	+0.38
JES	-4.27	+4.12	-4.95	+4.61
Low $\not{E}_T$	-3.60	+3.09	-4.61	+4.23
b-tag efficiency	0.60		0.62	
Mistag rate	0.27		0.29	
$t\bar{t}$ cross section	-0.12	+0.11	-0.07	+0.07
W+jets cross section	-0.17	+0.17	-0.10	+0.10
overall	5.65		6.81	

Table 9.3: Expected uncertainties on the measured m_{top} for $1/\text{fb}$ of integrated luminosity using a reconstruction without the kinematic fit. The top quark mass is extracted from the $m_{t\bar{t}}$ distribution as well as from the transverse $m_{t\bar{t}}$ distribution.

Table 9.3 shows the expected uncertainties using the reconstruction with the two alternative variables. As already discussed in Section 9.2.3 the uncertainty from the JES calibration is much higher without the use of the kinematic fit and the χ^2 cut. The overall uncertainty for both variables is thus higher than in the standard reconstruction for $m_{t\bar{t}}$. The transverse $m_{t\bar{t}}$ gives the largest uncertainty of 6.81 GeV. In summary, the transverse $m_{t\bar{t}}$ has the advantage of a simple definition which is contrasted to the disadvantage of a higher overall uncertainty.

10 Conclusions and Outlook

In this work a novel approach for a measurement of the top quark mass has been presented. The invariant mass distribution of the top-antitop quark system ($m_{t\bar{t}}$) is used to extract the top quark mass. This approach aims at avoiding theoretical uncertainties involved in common top quark mass measurements using the invariant mass of the top quark from 3-particle decays. The presented analysis makes a step towards a top quark mass measurement from an event shape variable as desired for a high precision top quark mass measurement from the theoretical point of view.

This work has shown that a measurement of the top quark mass from $m_{t\bar{t}}$ will be feasible with the CMS experiment. A robust and accurate method for a measurement of the top quark mass from $m_{t\bar{t}}$ has been developed and the expected accuracy has been evaluated.

The top quark mass measurement from $m_{t\bar{t}}$ presented in this analysis is based on a template method. The idea of the template method is to extract the top quark mass by comparing a measured kinematic distribution to template distributions with different top quark masses. Here, a binned log-likelihood method is used to compare the measured $m_{t\bar{t}}$ distribution with different template distributions. This work has shown that this method is stable and gives accurate results.

An important tool used for the reconstruction of $m_{t\bar{t}}$ is a kinematic fit. The kinematic fit varies the particle momenta measured in the detector in order to fulfill kinematic constraints from the top quark decay. The masses of the W bosons in the $t\bar{t}$ decay as well as the equality of the top and anti-top quark masses are used as constraints. In this analysis a resolution of 44 GeV for $m_{t\bar{t}}$ in the most populated region has been reached without using the top quark mass itself as a constraint in the kinematic fit. This resolution allows a detailed analysis of the shape of the $m_{t\bar{t}}$ distribution.

This analysis has further shown that the χ^2 from the kinematic fit is an essential handle for the reduction of combinatoric background as well as for the reduction of the systematic uncertainty from the Jet Energy Scale (JES) calibration. The impact of the JES uncertainty on the top quark mass (m_{top}) measurement has been reduced to

$$\frac{\Delta m_{top}}{\Delta \text{JES}} = 0.85 \frac{\text{GeV}}{\%} \ . \tag{10.1}$$

A crucial feature of the presented analysis is that it has been optimized with respect to the overall uncertainty at 1/fb of integrated luminosity. Since the overall uncertainty is dominated by systematic uncertainties, these have to be taken into account when choosing the optimal cuts used in the reconstruction of $m_{t\bar{t}}$. In this work an implementation of an optimization with respect to the overall uncertainty has been presented.

The expected experimental uncertainties for 1/fb of integrated luminosity are

$$\Delta m_{top} = \pm\, 0.53\ (\text{stat.}) \pm 2.51\ (\text{syst.})\ \text{GeV} , \tag{10.2}$$

where the JES calibration is by far the dominant source of uncertainties. A first crosscheck of the top quark mass, measured by the Tevatron experiments, with this method will thus be feasible with a rather small amount of integrated luminosity.

The extrapolation to higher integrated luminosities indicates that the invariant mass of the top anti-top quark system has the potential to becoming an essential handle for high precision top quark mass measurements.

List of Figures

List of Tables

List of Tables

Bibliography

[1] W. Wagner, Top quark physics in hadron collisions, *Rep. Prog. Phys.*, 68:2409–2494, 2005.

[2] F. Halzen and A. D. Martin, *Quarks and Leptons*, John Wiley and Sons, 1984.

[3] W.-M. Yao et al., The Review of Particle Physics, *J. Phys. G*, 33:1, (2006) and 2007 partial update for the 2008 edition.

[4] The Tevatron Electroweak Working Group for the CDF and DØ Collaborations, A Combination of CDF and DØ Results on the Mass of the Top Quark, 2007, hep-ex/0703034.

[5] A. Quadt, Top quark physics at hadron colliders, *Eur. Phys. J. C*, 48:835–1000, 2006.

[6] S. Abachi et al., Observation of the Top Quark, *Phys. Rev. Lett.*, 74:2632–2637, 1995, hep-ex/9503003.

[7] F. Abe et al., Observation of Top Quark Production in $p\bar{p}$ Collisions with the Collider Detector at Fermilab, *Phys. Rev. Lett.*, 74:2626–2631, 1995, hep-ex/9503002.

[8] H.L. Lai et al., *Eur. Phys. J. C*, 12:375, 2000, hep-ph/9903282.

[9] CMS Collaboration, CMS Physics Technical Design Report Volume II: Physics Performance, *CERN/LHCC*, 021, 2006.

[10] R. Frederix and F. Maltoni, Top quark physics in hadron collisions, 2007, hep-ph/7122355.

[11] M. Beneke et al., Top Quark Physics, 2000, hep-ph/0003033.

[12] S. Frixione and B.R. Webber, The MC@NLO 3.2 event generator, 2006, hep-ph/0601192.

[13] M.L. Mangano et al., ALPGEN, a generator for hard multi-parton processes in hadronic collisions, *JHEP*, 0307:001, 2003, hep-ph/0206293.

[14] S.R. Slabospitsky, Event generators for top quark production and decays, *CMS Conference Report*, 016, 2006, hep-ph/0603124.

[15] T. Sjöstrand et al., High-energy-physics event generation with PYTHIA 6.1, *Comput. Phys. Commun.*, 135:238, 2001, hep-ph/0010017.

[16] M. L. Mangano et al., Matching matrix elements and shower evolution for top-quark production in hadronic collisions, *JHEP*, 0701:013, 2007, hep-ph/0611129.

[17] CMS Collaboration, CMS Physics Technical Design Report Volume I: Detector Performance and Software, *CERN/LHCC*, 001, 2006.

[18] CMS Outreach, CMS Posters for Point 5, `http://cmsinfo.cern.ch/outreach/CMSdocuments/Point5Posters/CMSp5posters_index.html`.

[19] G. Jarlskog and D. Rein, *Large Hadron Collider Workshop: Proceedings Vol. I-III*, 1990.

[20] S. Agostinelli et al., GEANT4: A simulation toolkit, *Instrum. and Methods*, A506:250–303, 2003.

[21] R. Frühwirth, Application of Kalman Filtering to Track and Vertex Fitting, *Nucl. Instrum. and Methods*, A262:444, 1987.

[22] J.D'Hondt and P. Van Mulders, Measurement of jet energy scale corrections using top quark events, *CMS Analysis Note*, 029, 2007.

[23] R. Frühwirth and T. Speer, A Gaussian-sum filter for vertex reconstruction, *Nucl. Instrum. and Methods*, A534:217–221, 2004.

[24] S. V. Chekanov, Jet algorithms: A mini review, hep-ph/0211298.

[25] S. Esen et al., Plans for Jet Energy Corrections at CMS, *CMS Analysis Note*, 055, 2007.

[26] S. Esen et al., $\not{E}_T$ Performance in CMS, *CMS Analysis Note*, 041, 2007.

[27] A. Rizzi et al., Track impact parameter based b-tagging with CMS, *CMS Note*, 019, 2006.

[28] S. Lowette et al., Offline Calibration of b-Jet Identification Efficiencies, *CMS Note*, 013, 2006.

[29] M. Hansen et al., Top Quark Analysis Framework, *CMS Internal Note*, 068, 2007.

[30] Physics eXtension Library, `http://pxl.sourceforge.net`.

[31] R. Brun and F. Rademakers, ROOT - An Object Oriented Data Analysis Framework, *Nucl. Inst. & Meth. in Phys. Res. A*, 398:81–86, 1996, `http://root.cern.ch`.

[32] Work in progress in the CMS top quark Physics Analysis Group.

[33] M. Pierini and M. Spiropulu, Study $t\bar{t}$+jets as a function of jet p_T and multiplicity for 2007 1 fb^{-1} Monte Carlo production at CMS, *CMS Internal Note*, 038, 2007.

[34] M. Pierini and M. Spiropulu, Study of V+jets in bins of boson P_T and jet multiplicity for 2007 1 fb^{-1} Monte Carlo production at CMS, *CMS Internal Note*, 031, 2007.

[35] J. Cuevas et al., Measurements of the Top Quark Pair Production Cross Section with L= 100 pb^{-1} using the CMS Detector, *CMS Analysis Note*, 025, 2007.

[36] M. Erdmann et al., Measurement of the top quark pair invariant mass distribution, *CMS Analysis Note*, 027, 2007.

[37] J.D'Hondt et al., Fitting of Event Topologies with External Kinematic Constraints in CMS, *CMS Note*, 023, 2006.

[38] V. Blobel and E. Lohrmann, *Statistische und numerische Methoden der Datenanalyse*, B. G. Teubner, 1998.

[39] J.D'Hondt et al., Light quark jet energy scale calibration using the W mass constraint in single-leptonic $t\bar{t}$ events, *CMS Note*, 025, 2006.

[40] J. Rohlf and C. Tully, Recommendations for Jet and Missing Transverse Energy Reconstruction Settings and Systematics Treatment, *CMS Internal Note*, 000, 2006.

[41] V. Konoplianikov et al., Jet Calibration using γ+Jet Events in the CMS Detector, *CMS Note*, 042, 2006.

[42] R. Bonciani et al., NLL Resummation of the Heavy-Quark Hadronproduction Cross Section, 1998, hep-ph/9801375.

[43] J. Campbell et al., Production of a W Boson and Two Jets with One b-quark Tag, 2007, hep-ph/0611348.

Bibliography

78

Danksagung (Acknowledgements)

Als erstes geht mein Dank an Prof. Dr. Martin Erdmann für die ausgezeichnete Betreuung dieser Diplomarbeit. Die wöchentlichen Arbeitsgruppentreffen unter Leitung von Prof. Dr. Martin Erdmann, sowie die persönliche Betreuung waren hervorragende Vorraussetzungen für das Gelingen dieser Arbeit.

Prof. Dr. Thomas Hebbeker gilt ein großes Dankeschön für die Übernahme der Zweitkorrektur, sowie die Leitung der wöchentlichen Arbeitsgruppentreffen der 3A-CMS Gruppe.

Ganz besonderen Dank verdient Jan Steggemann für die hervorragende Betreuung während der gesamten Diplomarbeit. Seine große Hilfsbereitschaft bei physikalischen und technischen Fragen hat mir beim Erwerb aller nötigen Kenntnisse für diese Arbeit stark geholfen. Außerdem möchte ich mich für die stets angenehme Büroatmosphäre bedanken.

Danke auch an alle anderen Mitglieder der Arbeitgruppe – Matthias Kirsch, Anna Henrichs, Oxana Actis und Gero Müller – für die interessanten und lehrreichen Diskussionen in den wöchentlichen Arbeitsgruppentreffen und auch außerhalb der Treffen. Danke auch für die Einführung in die äußerst angenehme Kultur des Kaffees nach dem Mittagessen.

Außerdem möchte ich der 3A-CMS Gruppe – Dr. Kerstin Höpfner, Dr. Peter Kreuzer, Dr. Markus Merschmeyer, Dr. Arnd Meyer, Dr. Daniel Teyssier, Carsten Hof, Philipp Biallas, Jens Frangenheim, Michael Sowa, Clemens Zeidler, Holger Pieta und Walter Bender – für die wöchentlichen Diskussionen im Arbeitsgruppentreffen danken.

Für die Unterstützung bei technischen Problemen mit dem GRID und CMSSW gilt mein besonderer Dank – Dr. Thomas Kress, Dr. Andreas Nowak, Carsten Hof und Philipp Biallas.

Vielen dank auch an alle Korrekturleser – Prof. Dr. Martin Erdmann, Jan Steggemann, Matthias Kirsch, Philipp Biallas und Jens Frangenheim.

Yukiko, thank you for supporting me all the time! Thank you for everything!

Abschließend möchte ich meinen Eltern für die großartige Unterstützung während meines gesamten Studiums danken.